Mechanical compaction mechanisms in the input sediments of the Sumatra Subduction Complex-insights from microstructural analysis of cores from IODP Expedition- 362

Sivaji Lahiri[1]*, Kitty L. Milliken[2], Peter Vrolijk[3], Guillaume Desbois[1], Janos L. Urai[1]

[1]Institute of Tectonics and Geodynamics, RWTH Aachen University, Germany, Lochnerstrasse 4–20, 52056, Aachen, Germany

[2]Bureau of Economic Geology, The University of Texas at Austin, Austin, TX, 10611, USA

[3]Department of Earth and Environmental Science, New Mexico Institute of Mining and Technology, 801 Leroy Place, Socorro, NM 87801, USA

* Corresponding author: sivaji.lahiri2@gmail.com

Abstract

The input sediments of the North Sumatra subduction zone margin, drilled during IODP Expedition 362, exhibit remarkable uniformity in composition and grain size over the entire thickness of the rapidly deposited Nicobar Fan succession (seafloor to 1500 mbsf), providing a unique opportunity to study the micromechanisms of compaction. Samples were prepared from dried core samples from sites (U1480 and U1481) by both Ar-ion cross-section polishing and broad-ion beam cutting and imaged with a field-emission Scanning Electron Microscope (SEM). The shallowest samples (seafloor to 28 mbsf) display a sharp reduction in porosity from 80% to 52% due to collapse of large clay-domain/matrix pores associated with rotation and realignment of clay-platelets parallel to the bedding plane. The deeper succession (28mbsf to 1500mbsf) exhibits less rapid reduction in porosity from 52% to 30% by the progressive collapse of silt-adjacent larger pores through bending and subsequent sliding/fracturing of clay particles. In addition, there is a correlated loss of porosity in the pores too small to be resolved by SEM.

Clastic particles show no evidence of deformation or fracturing with increasing compaction. In the phyllosilicates, there is no evidence for pressure solution or recrystallization: thus, compaction proceeds by micromechanical processes. Increase in effective stress up to 18 MPa (~1500mbsf) causes the development of a weakly aligned phyllosilicate fabric mainly defined by illite clay particles and mica grains, while the roundness of interparticle pores decreases as the pores become more elongated. We propose that bending of the phyllosilicates by intra-particle slip may be the rate-controlling mechanism.

Pore size distributions show that all pores within the compactional force chain deform, irrespective of size, with increasing compactional strain. This arises because the force chain driving pore collapse is localized primarily

32   within the volumetrically dominant and weaker clay-rich domains; pores associated with packing around isolated

33   silt particles enter into the force chain asynchronously and do not contribute preferentially to pore loss over the

34   depth range studied.

1. Introduction

36   Muds are fine-grained sediments (>50% of particles <63μm diameter) comprising platy detrital clay minerals

37   and equidimensional detrital grains such as quartz, feldspar, calcite, etc. (Nakano, 1967; Hesse, R., 1975;

38   Sintubin, 1994). Understanding the mechanical, chemical, and microstructural properties of mud and mudstone

39   is of great interest for rock property prediction in basic earth science, in exploration, subsurface integrity studies

40   and geotechnical engineering (Yagiz, S., 2001; Aplin and Macquaker, 2011; Lazar et al., 2015). The chemical

41   and physical behavior of marine muds plays a critical role in defining the geometry of accretionary prisms,

42   locating the décollement for fault rupture (Vrolijk, 1990; Chester et al., 2013) and understanding subduction

43   zone earthquakes and tsunamis (Dean et al., 2010; Chester et al., 2013; Hüpers et al., 2017).

44   Marine mud is deposited with a highly porous isotropic fabric (Bowles, 1969; Bennett et al. 1981; 1991);

45   depositional porosity in mud is about twice as high as in sand (e.g., Velde, 1996, Lundegard, 1992). In contrast,

46   mudstones have low porosities, modal pore sizes measured in nm, and an absence of textural controls on porosity

47   (e.g. Aplin et al., 2006; Milliken et al., 2012; 2013). The processes in this dramatic evolution of porosity have

48   similarities to compaction of sand to sandstone, comprising a combination of compaction and cementation

49   (Milliken and Day-Stirrat, 2013), although the much smaller, elongated phyllosilicate grains increase the role of

50   clay-bound water in the process (Karaborni et al., 1996). Whereas a refined and somewhat predictive

51   understanding exists for porosity evolution in sand and sandstones (e.g., Lander and Walderhaug, 1999; Paxton

52   et al., 2002; Lander et al., 2008; Ajdukiewicz and Lander, 2010, Desbois et al., 2011), such a model is at best

53   preliminary for muds and mudstones (Pommer and Milliken, 2015; Milliken and Olson, 2017). It seems clear

54   that the composition of the grain assemblage importantly sets the stage for porosity evolution in muds (Milliken,

55   2014), cementation being the greatest in muds with abundant biogenic debris. In contrast to sandstones, however,

56   cementation is far less common globally in mudstones (Milliken, 2019), leading to the notion that mechanical

57   compaction may be far more important in muds. In addition, depositional environment also strongly controls

58   porosity evolution, compaction and diagenesis in mudrocks (e.g. Burland, 1990; Baruch et al., 2015; Delle Piane

59   et al., 2015) as the initial clay and rigid grain compositions significantly affect both compaction (as this

60   manuscript shows) and subsequent diagenetic alteration due to variations in composition. Establishing the

61   expected compaction behavior for muds in a setting of well-constrained mud properties is an essential

62   contribution that our study hopes to serve.

63   Investigations of mud and mudstone compaction are usually based on proxy data, such as velocity or density,

64   rather than direct measurements of porosity (e.g., references in Mondol et al., 2007). Direct measurement of

65   porosity is broadly classified into two categories: 1) experimental compaction in the laboratory; (e.g., Mitchell,

66   1956; Bennett et al. 1981; Griffiths and Joshi, 1989; 1990; Vasseur et al. 1995; Mondol et al. 2007; Fawad et al.

67   2010; Emmanuel and Day-Stirrat, 2012), and 2) studies on natural samples those are compacted in situ with

68   depth (e.g., Meade, 1964; Ho et al., 1999; Aplin et al. 2003; 2006; Day-Stirrat et al., 2008; 2010; 2012; Milliken

69   et al, 2012; 2013). A common shortcoming of the studies on the naturally compacted samples is the assumption

that the bulk porosity is a direct measure of compaction although porosity loss has contributions of both compaction and cementation (Ehrenberg, 1989; Lundegard, 1992; Paxton et al., 2002), and this can only be accomplished by petrographic inspection (Milliken and Curtis, 2016). Experimental studies generally avoid this shortcoming as the sample sets generally do not undergo any chemical change during the investigation. Studies of shallowly buried units (like the present study) are the ones most likely to avoid the complication of cementation, especially if temperatures are low and bulk grain assemblages are siliciclastic (Milliken, 2008, 2014).

Previous studies report contrasting ideas about the mechanisms of mechanical compaction of mud. Some studies conclude that rotation is the dominant particle scale mechanism for mechanical compaction (Bowles et al., 1969; Oertel and Curtis, 1972; Vasseur et al., 1995), although other particle scale-deformation mechanisms were not investigated by these authors. A few studies state that burial compaction significantly increases the alignment of phyllosilicate (clay and mica) parallel to the bedding planes (Bowles et al., 1969; Oertel and Curtis, 1972; Vasseur et al., 1995) (a detailed review of the previous studies on mechanical compaction is given in DocumentS1 in Supplementary data). Other studies suggest that intense mechanical compaction (i.e. effective stress) has a limited impact on the development of phyllosilicate fabric in mud (Ho et al., 1999; Aplin et al., 2006; Day-Stirrat et al., 2008; 2011). In addition, earlier authors concluded that an increase in effective stress causes preferential loss of larger pores, and as a result, the mean porosity of the samples decreases (Delage and Lefebvre, 1984; Griffiths and Joshi, 1989; 1990;Emmanuel and Day-Stirrat, 2012).With increasing consolidation stress, a bimodal pore size distribution curve shifts toward smaller pore sizes as larger pores rapidly collapse (Griffiths and Joshi, 1989; 1990; 1991). These studies investigated the changes in particle alignment and reduction in porosity (Ho et al., 1999; Aplin et al., 2006; Day-Stirrat et al., 2008; 2011) but without imaging the evolution of pore morphology with increasing compactional strain. Moreover, in previous studies, the authors mainly performed laboratory consolidation experiments on lab produced particle packs, and used conventional techniques, such as mercury intrusion porosimetry and high-resolution X-Ray pole figure goniometry (HRXTG) to understand the evolution of pore size distribution with consolidation stress (Ho et al., 1999; Aplin et al., 2006). Studies on naturally compacted samples are less common.

We received 55 mud samples from drill cores collected during IODP Expedition 362 west of the North Sumatra subduction zone margin and investigated the evolution of petrographic microstructure and pore morphology as a function of compactional strain. Apart from general implications for global mudrocks, we hope this investigation will also contribute to studies that seek to predict rock properties in the deeper subsurface at the Sumatra subduction front.

2. Geological background and drilling

The Sumatra subduction zone extends 5000km from the Andaman-Nicobar Islands in the northwest to the Java-Banda arc in the Southeast (Fig.1a and b) (Prawirodirdjo et al., 1997; Hippchen and Hyndman, 2008). The trench

105 of the Sumatra subduction zone (Fig.1a) developed on the subducting Indo-Australian Plate at a convergence

106 rate of 5.5 cm/yr in the north and 7.23 cm/yr in the South (Ghosal et al., 2014; Moeremans, and Singh, 2015).

107 On 26th December 2004, the west coast of Northern Sumatra recorded one of the largest earthquakes (Mw-9.3)

108 in the 21st century, generating a devastating tsunami in the Indian Ocean (Ammon et al., 2005; Lay et al., 2005).

109 Understanding the mechanism(s) behind this unprecedented event was the central idea behind IODP Expedition

110 362 (Fig.1). The main objective of the expedition was to collect core and log data from the incoming

111 sedimentary succession of the Indo-Australian oceanic plate to understand the seismogenic process related to the

112 margin (Dugan et al., 2017; McNeill et al., 2017a). During the expedition in 2016, drilling was performed on two

113 sites: U1480 (Holes E, F, G and H) and U1481 (Hole A) located on the oceanic plate west of the North Sumatra

114 subduction margin and east of the Ninety East Ridge (Fig.1a, b) (Dugan et al., 2017). The drilling sites recovered

115 a complete, 1.5 km thick sedimentary section from late Cretaceous to Pleistocene down to the basement of

116 basaltic crust (Dugan et al., 2017; McNeill et al., 2017a).

117 The input sedimentary section of the Sumatra subduction zone comprises the distal part of the trench wedge,

118 Nicobar fan sequence, and pre-fan pelagic section on the basaltic crust at the bottom (Dugan et al., 2017;

119 McNeill et al., 2017a). At Site U1480, the entire recovered section was categorized into six lithological entities,

120 Units I to VI (Fig. 1c) (McNeill et al., 2017a). Unit I (0 to 26.72 mbsf) consist of unconsolidated calcareous clay,

121 silty clay with alternating fine sand (McNeill et al., 2017a). Unit II from 26.72 to 1250 mbsf consists of three

122 subunits (IIA, IIB and IIC) and mainly exhibits alternating fine-grained sand and silty clay to silt (McNeill et al.,

123 2017a). Unit III (1250 ~ 1327 mbsf) is divided into two subunits: Unit IIIA and IIIB (McNeill et al., 2017a).

124 Unit IIIA consist of thin to medium-bedded, gray-green or brown mudstone and intercalated siltstone, and Unit

125 IIIB is composed of reddish-brown tuffaceous silty claystone with fragmented sponge spicules and radiolaria

126 (McNeill et al., 2017a). The boundary between Units IIIA and IIIB (1310 mbsf) at this site marks the base of the

127 Nicobar Fan and the beginning of the thin pre-fan succession (Pickering et al., 2020). Units IV, V, and VI

128 include volcanoclastic rocks with tuffaceous sandstone, conglomerates, and basaltic oceanic crust, respectively.

129 At Site U1481, the pre-fan succession was not encountered and a Unit III, a thicker equivalent of Subunit IIIA at

130 Site U1480, represents the material of the lower Nicobar Fan (see Figure F15, in Site U1481 report; McNeil et

131 al., 2017a). This study is restricted to the thin, distal trench wedge (Unit I) and Nicobar fan sequence (Units II

132 and IIIA, which is equivalent to Unit-III at U1481).

133 X-ray diffraction (XRD) of bulk samples and clay fractions at Site U1480 show a clay mineral assemblage

134 dominated by illite with lesser amounts of smectite and chlorite (Rosenberger et al., 2020) (Fig.2a, b, c, and d;

135 TableS1 and Figure S1 in Supplementary data). Clay mineral data arise from three separate analyses: (1) bulk

136 sample analyses of air-dried samples (random orientation) onboard ship used to define the proportion of all clay

137 minerals in a sediment sample(McNeill et al., 2017a; Underwood et al., 2020), (2) air-dried clay-sized samples

138 (sedimented and oriented) analyzed in New Mexico that define the types and abundances of clay

139 minerals(Rosenberger et al., 2020; note that abundances limited to clay minerals used in the reference mixtures,

140 which include discrete illite and discrete smectite), and (3) glycol-saturated clay-sized samples (sedimented and

141 oriented) analyzed in New Mexico that determine the amount of illite in mixed-layer I/S, defined as smectite in

142 #2 (Rosenberger et al., 2020). Note that the amount of illite in mixed-layer I/S is only accounted for in the
143 Expandability value and never in the discrete illite value.

144 Siliciclastic samples consist of 50-70% clay minerals (McNeill et al., 2017a). Smectite fraction, determined
145 from the air-dried, clay-sized samples (as described in Underwood et al., 2020) is more abundant in Unit I than
146 Unit II, where smectite abundance ranges from 5-30% with rare samples containing as much as 45% smectite.
147 In Unit II, smectite fraction ranges from 10-30% with local discreet enrichments as great as 40-45%. Smectite
148 again increases in Unit III, reaching a value as high as 68% in the samples attributed to the Nicobar Fan section.
149 There is a weak increase in the expandability of mixed-layer I/S with depth (determined from glycol-saturated,
150 clay-sized samples; Rosenberger et al., 2020; Underwood et al., 2020; Figure-S2 in Supplementary data),
151 suggesting a shift in clay mineral provenance rather than smectite-illite diagenesis. Montmorillonite is
152 interpreted as the smectite mineral (Rosenberger et al., 2020). Chlorite + kaolinite abundance is similar in Units I
153 and II, ranging from 8 to 20% with rare occurrences as high as 24%; Unit III is almost devoid of chlorite +
154 kaolinite. Heating experiments on select samples indicate that chlorite makes up 66-100% of this mineral
155 category (Rosenberger et al., 2020). Illite comprises the remainder of the clay mineral assemblage, ranging from
156 50-79% in Unit II while Unit I is correspondingly less illite-rich (42-70%). In the Unit III Nicobar Fan section,
157 illite makes up only 18-36% of the clay fraction. Again, it should be noted that, the shipboard methodology used
158 for XRD analysis is semiquantitative and has limitations in identifying bulk mineralogy of the samples; the
159 abundance of mixed-layer clays and the expandability of mixed-layer I/S is only inferred qualitatively (McNeil
160 et al. 2017a; Underwood et al., 2020).

161 The Nicobar fan sequence exhibits almost compositionally homogeneous (silt/clay ratio; mostly 'silty-clay')
162 subunits with uniform grain size (McNeill et al., 2017a), and a history of rapid deposition (125-290 m/my;
163 Backman et al., 2019). The sedimentary sequence exhibits no evidence of uplift and currently occurs at
164 maximum burial depth. The drilling sites are 255 km away from the deformation front; thus, the samples are
165 undisturbed by tectonic faulting associated with subduction (Fig.1b). In addition, owing to the scarcity of
166 biogenic grains and the low temperatures encountered (<68°C), cementation is only observed as highly localized
167 concretions (Red colored symbols in Fig.2e, f, g, and h) (McNeil et al., 2017b; Torres et al., 2022). Such a
168 homogeneous sedimentary succession extending across 1.5 km depth is rare in sedimentary basins. Hence, these
169 samples provide us with a unique opportunity to study depth-wise variation in microstructure as a function of
170 vertical effective stress with few complications from multiple causes of porosity loss.

171 **3. Sampling and Methods**

172 This study is based on two sample sets that were obtained from Sites 1480 (Holes E, F, G, and H) and 1481
173 (Hole A) independently and analyzed by slightly different methods. Samples have been prepared using Ar-ion
174 cross-section polishing and analyzed using a scanning electron microscope equipped with a field emission gun
175 (BIB-SE technique). The first sample set (33 mud samples; depth 1.24 to 1300 mbsf) was prepared and analyzed
176 at RWTH Aachen University, Germany. The second sample set (22 samples; depths 6.25 to 1493.30 mbsf) was
177 prepared and studied at the Bureau of Economic Geology (BEG) at the University of Texas at Austin. Respective
178 core description of these 55 mud samples and their bulk mineralogy data are tabulated in Table-1.

3.1 BIB-SEM technique (First set of samples, Aachen University)

3.1.1 Sample preparation for BIB-SEM and imaging

After drilling, the samples were stored at Kochi drill core repository (IODP), Japan for four years (2016 ~ 2020) in refrigerated storage areas, maintaining a temperature of ca. 4°C and 80% humidity (http://www.kochi-core.jp/en/iodp-curation/curation-sop_2.html). We received a total of 33 freeze-dried mud samples (SN-1 to SN-33 in Table-1) for analysis at Aachen. The samples were collected using a tube inserted perpendicular to the cut face of the drill core in such a way that the notch of the tube identified the top of the sample so the orientation of bedding planes for each sample was known. In Fig. 1d, a tube sample received from the IODP repository is shown, where the red line on the top of the tube identifies the notch. Subsamples ($10 \times 5 \times 2$ mm^3) were cut from the individual freeze-dried samples using a razor blade. These subsamples were pre-polished using silicon carbide (SiC) paper to reduce the roughness of the surface down to 10 μm. Further, Broad Ion Beam (BIB) polishing was carried out using a JEOL SM-09010 cross-section polisher for 10 hours at 6 kV and 150 μA. BIB reduces surface damage by removing a 100 μm thick layer to generate a high-quality polished cross-section of 1-2 mm^2 with topography less than 5 nm (Desbois et al., 2009).

After polishing, the BIB cross-sections were coated with tungsten and imaged with a Zeiss Supra 55 SEM with SE2, BSE, and EDX detector (Figure S3 in Supplementary data). SE2 images were used to image porosity and BSE images are combined with an EDX map as well as EDX point analysis for identifying mineral phases. For each cross-section, we made mosaics of hundreds of SE2 and BSE images at a magnification of 20,000x (~14.3 nm pixel value) and 10,000x respectively, with an overlap of 20% to 30%, (Klaver et al., 2012; 2015; 2016; Hemes et al., 2013; 2015; 2016; Laurich et al., 2014).The mosaics are stitched together using Aztec software preserving the original pixel resolution. Finally, these stitched images are used for the segmentation of pore spaces, minerals, and other respective analyses.

3.1.2 Image segmentation and pore analysis

For quantifying porosity and pore morphology, individual SE2 image mosaics were segmented using a 'seed and grow' algorithm (Adams and Bischof, 1994) implemented with a MatLab code (Jiang et al., 2015; Schmatz et al., 2017) (Figure S3 in Supplementary data). The 'seed and grow' algorithm works based on the difference in intensity of grey scale value in an image (bright = minerals, dark= pores). After automatic segmentation, individual pores in SE2 images are manually corrected if required.

Similarly, using ImageJ software (threshold toolbox and machine learning algorithm), segmentation of the individual mineral phases was carried out combining BSE images and EDX elemental maps. While quartz, calcite, pyrite, mica minerals are efficiently segmented using these tools, feldspars are found difficult to segment because of similar composition as clay (Figure S4, S5 and S6 in Supplementary data). Finally, corrected pore segmented SE2 mosaics are overlaid on the phase maps using the 'georeference' tool of QGIS (http://qgis.osgeo.org), (Figure S4, S5 and S6 in Supplementary data).

3.1.3 Pore detection resolution (PPR) and representative area analysis (REA)

'Practical pore detection resolution' (PPR) indicates the pore sizes above which one can assume to detect 100% of the pores present in the SE2 mosaic (Klaver et al., 2012). In agreement with earlier results using this instrument (Klaver et al., 2012; 2015; 2016; Hemes et al., 2013; 2015; 2016; Laurich et al., 2014), we found PPR of ~2000 nm^2 and ~8500 nm^2 for the magnification of 20,000x and 10,000x images, respectively, corresponding to 10pixels.

After segmenting all minerals, representative elementary area analysis (REA) was performed using the box counting technique on mineralogical phase maps (Kameda et al., 2006; Klaver et al., 2012). Similar steps are also followed for determining a representative elementary area for SE2 images. The estimated REA values using SE2 and BSE mosaics for the analyzed 33 mudstone samples are documented in Table S2 in Supplementary data.

Porosity, pore morphology, pore size, and the statistical distribution of pores were obtained using image analysis techniques on 2D images collected using BIB-SEM technique. Because pores are non-spherical 3D objects that are cut perpendicular to the bedding plane to acquire a 2D image dataset, there may be random and systematic errors when comparing 2D and 3D results. We plotted shipboard measured MAD (moisture and density) porosity vs depth (Fig.2e) and also BIB-SEM porosity vs depth for the analyzed samples (Fig.3a), where MAD porosity documents bulk porosity for the sample, and BIB-SEM porosity represents 2D cuts of the non-spherical 3D pores/porosity. As there is a first-order correspondence between the two porosity measurements, we deduce that porosity and pore size distributions obtained from 2D image analysis reflect the bulk rock porosity and 3D pore size distribution of the samples. In addition, the estimated REA appears appropriate for minimizing systematic errors in the bulk pore characteristics of the sample.

3.2 Ion polishing and SEM technique (second set of samples; BEG, UT Austin).

22 Samples (SN-34 to SN-55 in Table 1) were taken shipboard from the sample half of the still-wet core in small plastic tubes (similar to the ones used for the sample set at Aachen) inserted into the core by manual pressure. The tubes were removed from the core and sealed in plastic bags. In the laboratory at the BEG, sample bags were opened, and the muds were allowed to dry slowly in the tubes over several weeks. No discernible shrinkage was observed as the dried core pieces still fully filled the tubes. The tubes were carefully removed, and a small cube (approximately 0.5 to 1 cm^3) was cut using a sharp knife and small hand saws; an orientation mark was placed on the cube to indicate the bedding direction. Bed-perpendicular surfaces were prepared by Ar-ion cross-section polishing, using the Leica EM TIC020 triple ion beam miller and coated with Ir for imaging. Manual placement of the cut cubes into the ion mill is not precise so the ion-polished surfaces have slight variation from perpendicular to bedding. Pore imaging was performed on the FEI Nova NanoSEM 430 using the in-lens SE detector, a 30 μm aperture, 15 KeV accelerating current, a working distance of around 5–6 mm, and an intermediate-range sample current (spot size = 3nm, mid-range for the instrument). Randomly selected views (typically 3-6) of all samples were collected at 6000x machine magnification; additional views illustrating pore types and pore/grain relationships were made at 10,000x to 30,000x (machine magnification).

4. Results

4.1 Compaction strain derived from MAD-porosity data

During Expedition 362, mass and volume of mud samples were measured in both wet and dry states using a high precision electronic mass balance and helium pycnometer (http://www-odp.tamu.edu/publications/tnotes/tn37/ tn37_8.htm). Using the obtained mass and volume dataset for wet and dry conditions, bulk MAD (moisture and density) porosities were calculated. Porosity values reported by McNeill et al. (2017b) and downloaded from IODP databases serve as the basis for strain calculations.

Shipboard MAD porosity for mud samples exhibits a sharp reduction from 80% to 52% from the seafloor to 28 mbsf (Fig.2e). Deeper samples display a comparatively smaller reduction in porosity of approximately from 52% to 30% over a depth range of 28 to 1500 mbsf (Fig.2e and f).

We calculated compaction strain following a method proposed by Nollet et al. (2005) and subsequently used by Neagu et al. (2010) (Fig.2g and h), assuming 1D consolidation and no change in solid volume. The compaction strain (ε_c) is then computed as:

$$\varepsilon_c = \frac{1-\phi_0}{1-\phi_1} \qquad\qquad\text{(Eqn-1)}$$

Here ϕ_0 = initial porosity, and ϕ_1 = final porosity. Samples from sites U1480 and U1481 show no evidence of tectonic faults (McNeill et al., 2017a), supporting an assumption of 1D strain. We considered the initial porosity ϕ_0 as the MAD porosity at 0.6 mbsf depth ($\phi_0 = 80\%$). Compaction strain following Eqn-1 (Table S2 in Supplementary data), is plotted against depth in Fig.2g and h. Compaction strain increases from 1 to 2.05 from the seafloor to 28 mbsf (i.e. Unit I), and from 2.00 to 3.05 from 28mbsf to 1500 mbsf (Fig. 2g and h).

Another common measure of compaction is the intergranular volume (IGV; Paxton et al., 2002), which corresponds to the sum of intergranular porosity and intergranular cement. In some mudstones, it may be necessary to calculate IGV differently because of the presence of abundant primary intragranular pores and pore-filling bitumen (Milliken and Olson, 2017). In our sample set, cement is absent, and IGV is taken to equal the bulk porosity from shipboard MAD measurements.

Compactional porosity loss (COPL), referenced against the original sediment volume, is calculated from the initial primary intergranular porosity (Pi; 80% in this case) and the IGV as follows (Ehrenberg, 1989, Lundegard, 1992;):

COPL= Pi-(((100-Pi) x IGV)/(100-IGV))　　　　　　　　　　　　　　　　　(Eqn-2)

At an IGV of 50%, COPL is 60%; in the deepest samples in the Nicobar fan (IGV of around 30%) COPL is 70% (Table S2 in Supplementary data).

4.2 Description of grain microstructure and pore morphology

To have consistency in the data set, we prepared SE2 mosaics for all samples from the Aachen sample set at 20,000x magnification covering an average 100×100 μm^2 area. In addition, to examine the effect of magnification on BIB-SEM porosity and representative area analysis (REA), three samples (i.e. SN-7, SN-15, and SN-29) were also imaged each at 5,000x and 10,000x magnification, respectively. A decrease in magnification and resolution reduces visible BIB-SEM porosity.

We observed consistent results for the REA analysis. For SE2 mosaics, REA varies between $45 \times 45 \mu m^2$ to 85×85 μm^2 at 20,000x magnification, and for segmented phase maps, REA varies between 90×90 μm^2 to 130×130 μm^2 at 10,000x magnification. In the UT sample set, the standard images taken at 6000x with machine magnification are 49.7×45.7 μm^2, so these images are also within the estimated REA range.

Based on EDX elemental map or point analysis, six mineral phases occur in significant amounts in the Sumatra samples: quartz, feldspar (K-feldspar, Na-feldspar), calcite, pyrite, micas (muscovite, biotite, and chlorite), and clay. Based on XRD analyses (Rosenberger et al., 2020), the clay size fraction is dominated by illite. Clay + mica percentage in these mudstone samples varies between 65% to 75%. Samples SN-1 (77%) and SN-4 (76%) have more clay + mica, whereas SN-7, SN-9, SN-17, SN-28, SN-29, and SN-31 contain less clay + mica (<65%) (Table S2 in Supplementary data). It should be noted that, using EDX analysis, we are able to differentiate Na-feldspar, and K-feldspar considering the concentration of Na and K elements in the grains. However, the XRD dataset provides only information about the overall percentage of plagioclase feldspar present in these samples (Table 1), perhaps an artifact of different detection limits for EDX and XRD analyses.

Using BIB-SEM and automatic pore segmentation techniques, an average of >30,000 pores have been detected for each individual sample in the Aachen sample set at 20,000x magnification. Correlating with the MAD data set, the estimated BIB-SEM porosity reduces from 32% to 19% over a depth range of seafloor to 28 mbsf, while the deeper samples display a smaller reduction from 19% to 10% over a depth range of 28 to 1500 mbsf respectively (Fig.3a). Consistent with numerous previous studies, the results document a mismatch between bulk measured porosity (MAD) and imaging porosity (BIB-SEM) (e.g., Hemes et al., 2013; Houben et al., 2014; Nole et al., 2016; Oelker et al., 2019) (Table S2 in Supplementary data). We plotted BIB-SEM porosity vs MAD porosity and found an approximately linear correlation with coefficient of determination ($R^2 = 0.8621$) (Fig. 3b). It should also be noted that, although there is a correlation, there is a large difference in the porosity values which increases with increasing porosity.

4.3 Type of pores

Intergranular pores contribute >99% of the total visible porosity. Intragranular pores (see below) are rare. The size and shape of intergranular pores change during compaction (Table S3 in Supplementary data).

Intergranular pores are classified (Fig.4) based on the size of surrounding particles (irrespective of mineralogy): 1) Clay domain (matrix) pores, and 2) silt-adjacent pores. Based on the variation in size, clay domain pores are divided further into: 1) Large clay domain pores (pore size $>5 \times 10^5$ nm^2) and the pore boundary is defined by

315   more than three clay particles; and 2) small clay domain pores (pore size $<5\text{x}10^5$ nm^2) that occur between 2-3

316   clay particles (see further details below). Large and small clay domain pores are classified by geometry as: 1)

317   Elongate pores (aspect ratio $>3{:}1$) and 2) equant-shaped pores (aspect ratio $<3{:}1$). Elongate pores consist of 1)

318   Linear-elongated pores, and 2) crescent-shaped elongated pores. Examples of different clay-domain pore types

319   are shown in Fig. 5, 6, and 7.

320   Silt-adjacent pores are categorized by two types: 1) large silt-adjacent pores are $>5\text{x}10^5$ nm^2, and pore

321   boundaries are defined by more than three particles; and 2) small silt-adjacent pores include pore sizes $<5\text{x}10^5$

322   nm^2, and pore boundaries are defined by two/three particles (see further detail on the modal sizes of these pore

323   types below). Large and small silt-adjacent pores are either: 1) Equant shaped (aspect ratio $<3{:}1$) or 2) elongated

324   (aspect ratio $>3{:}1$). Further, elongated silt-adjacent pores consist of 1) linear-shaped elongated pores and 2)

325   crescent-shaped elongated pores. These pore types are highlighted in Fig. 5, 6, and 7.

4.4 Change in inter-particle pore morphology with depth

Seafloor to 28mbsf (Unit I)

328   The shallow mud samples in Unit I are unconsolidated andporous (Fig. 5a). We analyzed a total of 10 samples (6

329   samples at Aachen and 4 samples at UT Austin) from this depth range. Among them, two samples have been

330   analysed both in Aachen as well as in Austin, respectively. Sample SN-1 (1.24 mbsf) has a maximum MAD

331   porosity of 80%. We observe three types of clay particle contacts in the microstructure of SN-1; edge to edge

332   (EE), edge to face (EF), and face to face (FF) contacts (Table S4 in Supplementary data). Among them, EF and

333   FF contacts are abundant and EE contacts are rare. The sample exhibits abundant large clay domain pores and

334   large silt-adjacent pores that are equant with smooth edges and a rounded pore perimeter. The sample also

335   contains abundant linear-elongated and equant-shaped small clay-domain pores. Crescent-shaped small clay

336   domain pores are rare in the microstructure of this sample. Equant-shaped, small silt-adjacent pores are

337   abundant. In addition, linear elongated and crescent-shaped small, silt-adjacent pores are also common (Fig.5a;

338   Table S3 in Supplementary data).

339   With increasing compaction strain ($\varepsilon_c = 1.119$) and depth (5.1 mbsf; Figure S7 in Supplementary data), porosity

340   (MAD) reduces to 75% and corresponding COPL=19% (sample SN-2; Fig. 5b, Table S2 in Supplementary data).

341   The microstructures of SN-2 display similar characteristics to those observed in sample SN-1, although there are

342   fewer large clay domain pores in SN-2 than SN-1. Linear elongated and equant-shaped small clay domain pores

343   are common Table S3 in Supplementary data), but crescent-shaped small clay domain pores are rare. The

344   microstructures of SN-2 exhibit abundant equant-shaped large and small silt-adjacent pores.

345   With an increase in compaction strain to $\varepsilon_c\sim2.00$ (28 mbsf), the sample microstructure is dominated by FF

346   contacts (Fig. 5e), and EE and EF contacts are rare (Table S4 in Supplementary data). Additionally, large clay-

347   domain pores become infrequent in the microstructure (Fig.5e and Fig. 8). Crescent-shaped, small clay domain

348   pores in the microstructure are rare, whereas equant-shaped small clay domain pores are common. Both small

349   and large silt-adjacent pores exhibit equant shapes (Fig.5e and Fig. 8d, e, f). The sample analyzed at the base of

350   Unit I (SN-6; 28 mbsf) contains rare large clay-domain pores and abundant FF contacts (Fig. 5c; MAD porosity

351   = 54% and COPL = 55%).

28 mbsf to 1500 mbsf (Units II and III)

353 Mud samples from the Nicobar fan section are more compacted than shallower samples (Fig. 6, 7 and Figure S8

354 in Supplementary data). We analyzed a total of 29 samples using at Aachen and 18 samples at UT Austin from

355 this section. An increase in compactional strain from 2.00 to 3.15 over a depth range of 28 to 1500 mbsf causes a

356 porosity reduction (MAD) of 54% to 28%, and the corresponding change in average COPL is 55% to 72%. The

357 microstructure of these samples is dominated by FF contacts among clay particles; EF and EE contacts are rare

358 (Table S4 in Supplementary data; Fig. 6 and 7 b, c). All samples exhibit abundant small linear-elongated clay

359 domain pores between two parallel clay sheets (Fig. 8b). Equant-shaped small, clay domain pores are rarely

360 observed below 150 mbsf depth (ε_c>2.4). Crescent-shaped, small, clay domain pores are rare at shallow depth

361 but become abundant with an increase in compactional strain ε_c>2.95 (871.87 mbsf) as the surrounding clay

362 particles are bent (Fig.6). In addition, large clay domain pores in these samples are rarely observed in the vicinity

363 of silt clasts (Fig.6).

364 Below 100 mbsf (ε_c=2.20), silt-adjacent small pores are dominantly equant shaped, but below 300 mbsf (ε_c>2.5)

365 silt-adjacent small pores are dominantly linear-elongated (Fig. 8e). Crescent-shaped, small, silt-adjacent pores

366 are common in all samples. Large silt-adjacent pores are dominantly equant above 200 mbsf depth (ε_c<2.40) and

367 commonly linear-elongate below 400 mbsf depth (ε_c>2.5) (Fig.8f). It appears that due to an increase in

368 compactional strain, the shape of the silt-adjacent pores changes from equant to linear-elongated (Table S3 in

369 Supplementary data). In samples with more silt, equant-shaped small and large, silt-adjacent pores can persist at

370 greater depths (Fig. 8e and f).

371 Below 28 mbsf (ε_c>2.0), the number of large silt-adjacent pores in the microstructures decreases. Comparing

372 samples SN-8 (74.07 mbsf and ε_c=2.09) and SN-33 (1299.14mbsf and ε_c=2.51) illustrates how the number of

373 large, silt-adjacent pores decreases with depth (Fig. 6a, and c) when the clay fraction (Table S2 in

374 Supplementary data) is comparable. This relationship is apparent even in samples separated by a smaller depth

375 difference (SN-49 from 959.14 mbsf and SN-55 from 1433.36 mbsf; Fig. 7b and c). While the number of large

376 pores diminishes, the maximum size of the large silt-adjacent pores remains constant (10^7 nm^2; Figure S9).

377 It can be observed in Fig.2e that, around 1300 mbsf depth MAD porosity for the sample sets again rapidly

378 increases. However, microstructural observations of the sample from this horizon does not exhibit increase in

379 porosity (Fig. 6c). Hence, the increase in MAD porosity in this horizon is attributed to the increase in smectite

380 content (Fig.2a) (Dutilleul et al., 2021). In general, the moisture and density method (MAD) overestimate the

381 measured porosity of the smectite rich sediment because of the inclusion of the interlayer water from smectite

382 during measurement (Brown and Ransom, 1996; Dutilleul et al., 2020).

383 **4.5 Variation in the orientation of pores and grains due to compactional strain**

384 We examined the change in orientation of the long axis of pores with increasing compaction strain. For all

385 segmented pores, the angle between the long axis and the bedding plane was determined and plotted in rose

386 diagrams (Supplementary data-15). Samples from the seafloor to 28 mbsf exhibit a weak preferred orientation of

387 the long axis of pores with maxima oriented obliquely to the bedding planes. However, below 28 mbsf the

samples have a preferred orientation of the long axis of pores aligned subparallel to the bedding plane.Further, due to an increase in vertical effective stress down section below 28 mbsf in Units II and III, the degree of preferred alignment of the long axis of pores only increases by a small amount (Figure S10).

We determined the angle between the long axis of individual silt grains and the bedding plane for all samples and plotted the angle in a rose diagram (Figure S10). For quartz, feldspar, and calcite the degree of preferred orientation of the long axis of grains changes little with depth. However, the rose diagrams obtained for mica show weak maxima parallel to the bedding plane and several submaxima oriented obliquely to the bedding plane above 28 mbsf. Preferred alignment of the long axis of mica grains increases at 28 mbsf with a strong maximum oriented parallel to bedding plane. Below 28 mbsf, further increase in the degree of preferred alignment is small.

4.6 Size distribution of pores

Pore size distributions (Fig.9) of shallow samples (Unit I) are trimodal. Sample SN-1 has peaks between 10^5 to 10^6 nm^2, 10^6 to 10^7 nm^2, and 10^7 to 10^8 nm^2, and SN-2 has peaks from 10^4 to 10^5 nm^2, 10^5 to 10^6 nm^2, and 10^6 to 10^7 nm^2. These three pore size regimes correspond to the small clay domain and silt-adjacent pores, large clay domain pores, and large silt-adjacent pores. Samples of Units II and III exhibit bimodal pore size distributions (SN-10, SN-26, and SN-33 in Fig.9). SN-10 has a peak between 10^5 to 10^6 nm^2, corresponding to small clay domain and silt-adjacent pores, and 10^6 to 10^7 nm^2, reflecting large silt-adjacent pores. Large clay domain pores are absent from samples below 28mbsf depth (Units II and III) based on the pore size distributions combined with image analysis. At shallow depths, the contribution to total porosity by larger silt-adjacent pores is greater compared to the contribution by small clay domain pores (Fig.9e and g). The contribution of large, silt-adjacent pores to total porosity diminishes with depth. Hence, at greater depth, contribution to total porosity by larger silt adjacent pore is less compared to small clay domain pores (Fig.9i).

Pore size distributions follow a power-law shown on a double logarithmic graph following the equations (Klaver et al., 2012; 2015; 2016; Hemes et al., 2013; 2015; 2016; Laurich et al., 2014):

$$\frac{N_i}{b_i S_{mosaic}} = C S_{Pore}^{D} \qquad \text{(Eqn-3)}$$

$$\log\left(\frac{N_i}{b_i S_{mosaic}}\right) = -D.\log\left(S_{pore}\right) + Log\ C \qquad \text{(Eqn-4)}$$

Where N_i= number of pores with area S_{pore}, b_i= bin size, S_{mosaic}= surface area of the current mosaic, C=constant, and D= power-law exponent. The resulting power-law exponent (D) varies between 1.70 to 2.00 (Table T2 in Supplementary data).

4.7 Effect of texture on porosity, pore morphology, and orientation of pores

We analyzed six samples (SN-7, SN-9, SN-17, SN-28, SN-29, and SN-31) that are enriched in silt content compared to the rest of the mud samples (Table T2 in Supplementary data)). Silt content has a positive correlation to the total SEM porosity. For example, sample SN-29 (1172.88 mbsf) exhibits a BIB-SEM porosity of 14% whereas other samples from a similar depth with less silt exhibit an average BIB-SEM porosity of 12%

12

421 (Table T2 in Supplementary data) at 20000x magnification. The samples with greater silt content are also

422 enriched in equant-shaped silt-adjacent larger pores (Fig.10a). We also estimated the orientation of the long axis

423 of pores for these three samples and plotted the obtained results as rose diagrams (Fig.10b). The obtained results

424 exhibit a relatively weak preferred alignment of the long axis of pores with respect to the bedding planes

425 (Fig.10b).

426

427 **5. Discussions**

428 **5.1 Effective stress vs porosity: A comparison with experimental study**

429 To understand the consolidation mechanisms of the Sumatra sediments, we estimated vertical effective stress

430 following the steps proposed by Hüpers et al. (2015). Following Terzaghi and Peck (1948), vertical effective

431 stress (σ_v') is expressed as:

432 $\sigma_v' = \sigma_v - P_f$ (Eqn-5)

433 Here σ_v = total vertical stress caused by the overburden load, and P_f = fluid pressure. To compute vertical

434 effective stress of a layered sediment, we useEqn6:

435 $\sigma_v' = \sum(\boldsymbol{\rho_s} - \boldsymbol{\rho_w}) \cdot \mathbf{g} \cdot \boldsymbol{\Delta z}$ (Eqn-6)

436 where $\boldsymbol{\rho_s}$ = bulk density of the sediment, $\boldsymbol{\rho_w}$ = density of the pore water, $\boldsymbol{\Delta z}$ = depth interval, and g= gravitational

437 acceleration. Although small offset strike-slip faults are evident at the seafloor and in seismic reflection profiles

438 (McNeill et al., 2017a), the amount of strain attributed to these fault offsets supports the idea that the maximum

439 horizontal stress is comparable to the vertical stress; there is no evidence in seismic reflection data or from core

440 microstructures for thrust or reverse faults associated with a vertical least principal stress. On this basis, we

441 assume that vertical stress is the maximum principal stress, and that pore pressure is hydrostatic. Bulk density of

442 the sediment $\boldsymbol{\rho_s}$ was acquired from MAD data set obtained from IODP website (McNeill et al., 2017a), and $\boldsymbol{\rho_w}$

443 was considered as the density of seawater i.e. 1025 kg/m^3 (Hüpers et al., 2015).

444 We plotted vertical effective stress against MAD porosity for 55 mud samples (Fig.11). Fawad et al. (2010)

445 experimentally studied the consolidation behavior of mud with varied proportions of silt and clay. While

446 Sumatra samples follow trends like those defined by Fawad et al. (2010), the experimental samples are more

447 compacted than natural Sumatra samples for the same silt content.

448 Clay mineralogy has a significant effect on the compaction behavior of mudstone (Mondol et al., 2007). Mondol

449 et al. (2007) performed compaction experiments using pure smectite and pure kaolinite clay particle packs

450 because they represent two end members compared to other clay minerals (illite and chlorite) in terms of grain

451 size and surface area. Smectite is the more fine-grained clay with the largest surface area while kaolinite is

452 coarser and has a smaller surface area than other clay mineral types (Meade, 1964; Mesri and Olson, 1971; Rieke

13

453 and Chilingarian, 1974).Kaolinite is more compressible than smectite, and clay compaction gradually decreases

454 with increasing the proportion of small size clay particles in the sample (Mondol et al, 2007).

455 Fawad et al., (2010) used clay mixtures of 81% kaolinite, 14% mica, and 5% microcline grains, whereas Sumatra

456 mud samples are composed of 50%-79% illite and 5%-30% smectite, with only 8-20% undifferentiated chlorite

457 and kaolinite and 5-10% quartz particles. Therefore, due to higher illite and smectite content, Sumatra muds

458 appeared to be less compacted than the experimental samples used by Fawad et al. (2010).

459 **5.2 BIB-SEM porosity vs MAD porosity**

460 We note that BIB-SEM porosity is lower than the porosity found from shipboard MAD data, however the two

461 measurements correlate along a line through the origin. (Fig.3b). The reason for this difference is that MAD

462 porosity measures the total amount of moisture in a much larger sample and accounts for pores much below the

463 PPR. Rare large pores are also under-represented in the 1 mm^2 BIB section. Earlier studies also documented and

464 discussed mismatches between MAD and BIB-SEM measurements (Hemes et al., 2013; Houben et al., 2014;

465 Nole et al., 2016; Oelker et al., 2019).They concluded that the mismatch could be due to several factors; i) BIB-

466 SEM porosity largely depends on the magnification and resolution of images, ii) variation in sample sizes, and

467 iii) MAD porosity takes into account the pores whose sizes are much lower than PPR, whereas BIB-SEM

468 technique detects only the pores larger than PPR. We plotted estimated BIB-SEM porosity and MAD porosity

469 data from earlier studies on Boom clay (Hemes et al., 2013; Oelker et al., 2019); Opalinus clay (Houben et al.,

470 2014) and samples from the Nankai trough (Nole et al., 2016). The data for Boom clay and Opalinus clay follow

471 a similar trend to the Sumatra samples, whereas clay samples from the Nankai trough shows a different trend.

472 This difference may be attributed to differences in magnification of Nankai trough samples.

473 In addition, we plotted clay content against the difference between the two porosities in Fig.12a. We performed

474 regression analysis using the data set for the 33 mud samples analyzed at Aachen (Fig.12b) for BIB-SEM

475 porosity versus MAD porosity (following Eqn-7) but also incorporating the effect of clay content (following the

476 Eqn-8).

477 BIB-SEM porosity=a*MAD porosity + c   (Eqn-7)

478 BIB-SEM porosity =a*MAD porosity +b*clay content + c   (Eqn-8)

479 The coefficient of determinations (R^2) for Eqn-7 and Eqn-8 are 0.7126and 0.9262 respectively. These results

480 suggest that theratio in porosity depends on depth and clay content.

481 For all samples, the BIB-SEM pore size distribution follows a power-law over an interval of three orders of

482 magnitude. We may extrapolate this below the practical pore resolution (PPR; Klaver et al., 2012; Kuila and

483 Prasad, 2013; Wang et al., 2019). Extrapolating our data set down to 3nm pore diameter, the BIB-SEM porosity

484 increases only up to 20%~25%. A mismatch of 15% to 20% between the MAD porosity and extrapolated BIB-

485 SEM porosity remains. The fall -off from the normal trend in log-log pore size distribution plots (Fig.9b) for the

486 shallow depth (Unit-I) samples suggest that also large pores are also under-counted in the data set. The mud

14

487 samples from Unit-I contains forams that are rare or absent in the deeper section (Figure S11 a, b, c, and d in
488 Supplementary data), and part of missing pore volume can be attributed to the intact forams that may be missed
489 due to the small size of the BIB SEM sample.

490 Another factor that can create a mismatch between data sets is drying artefacts. In the past, Desbois et al. (2014)
491 performed a detailed study on drying artefacts of mudstone samples using Cryogenic BIB-SEM technique. They
492 identified four types of drying damages (Type-I, II, III and IV) that can develop during drying of a mudstone.
493 Type-I and type-II drying damage develops at clay/clay particle interfaces with tip to long axis contact, and at
494 clay/clast interfaces. Heterogeneous deformational behavior or shrinkage strain of clay and/or non-clay mineral
495 grains can cause a build-up in stress at the boundary between particles during drying. Type-III drying artefacts
496 are large cracks that develop within the clay matrix itself. Type-IV drying artefacts are the small damages that
497 modify pore morphology during drying. Among all of them, Type-II and III are the most spectacular and large
498 enough to modify microstructure significantly. The morphology of the type-II and III drying artefacts are
499 characterized by large irregular shaped very elongated pores with serrated pore boundaries. However, in the
500 present study, the large clay domains and silt-adjacent pores in all samples potentially show smooth edges and
501 rounded pore tip-end, which are incompatible with the typical morphologies of the drying artefacts (Fig.5, 6 and
502 7). Hence, drying artefacts appear to be less important for reconciling a mismatch between MAD and BIB-SEM
503 porosity.

504 Shallow samples from Unit-I are richer in smectite content than deeper samples, although a few samples from
505 400to 1000 mbsf have similar smectite abundances as Unit I.The moisture and density method (MAD) may
506 overestimate the measured porosity of the sediment if interlayer water from smectiteis included in the
507 measurement (Brown and Ransom, 1996; Dutilleul et al., 2020). Greater smectite content in the shallow samples
508 (Unit-I) may have contributed to an overestimation of the MAD porosity in the study. This is also consistent with
509 the observation that the difference between the measurements getting larger as porosity increases.

510 **5.3 Micromechanical model for porosity reduction**

511 **5.3.1 Sharp reduction in porosity at the shallow depth from the seafloor to 28 mbsf**

512 High porosity (80% MAD; 32% BIB-SEM) in the shallowest sediments is attributed to large pores in the
513 samples created by abundant EE and EF particle contacts (Fig. 5a and 7a). These contacts are unstable and
514 collapse under low effective stress to form FF contacts, resulting in a rapid porosity decrease within the first 28m
515 of burial (Supplementary data-11). This deformation is apparent from the reduction of large clay domain pores
516 observed over this interval (Fig. 8; Supplementary data-10). Collapse of pores surrounded by EE and EF
517 contacts is further recognized by the progressive alignment of clay particles into the bedding plane, which
518 promotes an increase in the number of elongated, small, clay domain pores parallel to the bedding plane. Each
519 of these observations is consistent with rotation of clay particles into the bedding plane as these large clay-
520 domain pores collapse.

5.3.2 Mechanism of porosity reduction from 28 mbsf to 1500 mbsf

Below 28 mbsf to >1500 mbsf, porosity continues to decrease from 52-30% (MAD) but at a reduced pace. SEM observations suggest that this porosity decline results from the progressive loss of silt-adjacent pores with large silt-adjacent pores lost before small ones (Fig. 8), although they remain present in common abundance to1200 mbsf. Small clay domain pores are abundant throughout the section, and the large clay domain pores are lost between the seafloor and 28 mbsf.

Within the population of silt-adjacent pores, the large, equant pores are most susceptible to collapse (Fig. 8). Large, elongate pores persist in abundance, both in linear and crescent geometries. While it seems plausible that large, equant pores collapse to form large, elongate pores, no corresponding increase in the elongate pore population is observed. Large, elongate pores may collapse further and become small silt-adjacent pores. Microstructural evidence supports the idea that large equant pores collapse as surrounding clay particles within clay-rich domains bend and shrink the size of the remaining pore (Fig.13), and that the collapse results in an increasing aspect ratio of the pore.

Frequently, bent clay particles are observed on the top of larger silt-adjacent pores. In the clay microstructure, large silt-adjacent pores act as a zone of heterogeneous strain localization. Clay particles can bend and collapse into large silt-adjacent pores more readily than the smaller pores in the clay matrix (Fig.13a to f). With increasing vertical effective stress two situations can arise which are demonstrated in the model shown in Fig.13g. First, with an increase in effective stress, the bent clay particles can lose frictional resistance from the sidewall (Fig.13a and b), can continue to bend, and slide down to fill the larger silt-adjacent pore space (Fig.13g-(iii)). Second, with an increase in vertical effective stress, bent clay particles may develop fractures (red lines in Fig.13g-(iv)) and subsequently collapse into the larger silt-adjacent pore space to reduce the porosity of samples (Fig.13g-(v)). Fig.13a represents fractured bent clay on the top of the larger silt adjacent pore (shown by white arrow). Similarly, two small clay particles appear to have fallen into the larger silt adjacent pore space (Fig.13e) while another bent clay particle (shown by white arrow) covers the pore. Fig.13f represents a bent clay particle wrapping across the top of twoquartz particles, and four small clay platelets fill the space between two quartz particles, suggesting an older larger silt-adjacent pore filled by fractured clay platelets. Occurring within the pore space between two equant quartz grains (Fig.13f), four small clay particles appear to have developed due to the fracturing of two large bent clay particles. Hence, it appears that the collapse of larger silt-adjacent pores in these mud samples is governed by the bending of clay particles and subsequent fracturing due to an increase in vertical effective stress. While these processes are defined within individual pores, the observed deformation is interpreted to result from an imposed force chain that acts on specific pores in a progressive manner as the force chain evolves and as adjacent pores deform.

Small silt-adjacent pores also become less abundant with burial, but the transition occurs deeper than the large pores, and small, silt-adjacent pores remain common throughout the section (Fig. 8; Supplementary data-11). Small equant pores are lost like the large pores, and elongate pores remain abundant within this population subset throughout. There is a loose correspondence between the loss of small, equant pores and an increase in elongate pores, suggesting that pore flattening is part of the pore collapse history. The pore collapse evolution

558   outlined for large pores (Fig.13g) appears to also hold for small pores, even though observations are more

559   challenging.

560   Small, clay domain pores appear to remain resilient throughout the compaction history (Fig. 8), even though

561   some of these pores must become lost to account for porosity loss. Small, equant pores are lost between 100-200

562   m, and this loss appears to be accommodated by an increase in elongate pores (Fig. 8). Elongate crescent pores

563   increase in abundance around 800 mbsf, and we interpret this to reflect folding of abundant linear elongate pores

564   as the overall system compacts.

565   Large equant pores in the clay domain are lost within the first few 10's of meters of burial. Elongate pores

566   appear to form at the expense of equant pores, and there may be a reduction in pore size associated with this

567   shape change. Most of the pores remaining after 1500 m of burial are small, elongate pores found both in clay

568   domain and silt-adjacent pores.

569   The presence of silt particles locally redistributes the force chain of load to retain undeformed, silt-adjacent,

570   large pores (Schneider et al., 2011). The samples with greater silt content are also enriched in equant-shaped silt-

571   adjacent larger pores (Fig.10) in the microstructure. Hence, as a result, they display greater porosity compared to

572   other samples from similar depth intervals (Fig.10).

573   Previous studies report contrasting ideas on the development of phyllosilicate fabric strength due to mechanical

574   compaction. Some studies suggest that mechanical compaction creates a phyllosilicate fabric in mud (Bowles et

575   al., 1969; Oertel and Curtis, 1972; Vasseur et al., 1995), whereas other studies conclude that vertical effective

576   stress has limited impact on phyllosilicate fabric development (Ho et al., 1999; Aplin et al., 2006; Day-Stirrat et

577   al., 2008; 2011). Here, we consider the preferred orientation of pores as a proxy for the alignment of

578   phyllosilicate (Hemes et al., 2013). At shallow depth (Unit-I), a weak preferred alignment of the long axis of

579   pores with maxima oriented obliquely to the bedding planes is formed (Supplementary data-15), and at greater

580   depth (Unit-II and III) the long axes of pores become aligned subparallel to the bedding plane. Increase in

581   vertical effective stress below 28mbsf depth creates only a small increase in the preferred orientation of the long

582   axis of pores. Hence, we found only a limited change in phyllosilicate fabric strength with increasing vertical

583   stress.

584   Previous authors also document the evolution of pore size distribution in mud with an increase in consolidation

585   stress using laboratory experiments and mercury-intrusion porosimetry (Griffiths and Joshi, 1989; 1990). They

586   conclude that the pore size distribution appears to be bi-modal, and the distribution curve shifts toward smaller

587   pore sizes with an increase in applied consolidation stress (Griffiths and Joshi, 1989). We observe an initial

588   transition from tri-modal to bi-modal pore size distribution around 28mbsf depth due to rapid collapse of large

589   clay domain pores by compactional strain. With an increase in depth below 28mbsf, the bi-modal pore size

590   distribution persists and tends to shift toward small pore sizes as the number of larger silt-adjacent pores

591   diminishes.

592   Laboratory studies have emphasized the importance of clay particle rotation as a dominant mechanism for

593   mechanical compaction in mudstone (Bennett et al., 1981, 1991; Vasseur et al., 1995; Aplin et al., 2006; Day-

594   Stirrat et al., 2008; 2011). We observe particle rotation only in the shallowest samples where unstable EE and EF

595   particle contacts are present. Clay particle bending and sliding/fracturing are considered more important for most

596   of the section studied.

597   **5.3.3 Mechanical compaction of marine sediment: a conceptual model**

598   According to earlier studies (Delage and Lefebvre, 1984; Griffiths and Joshi, 1989; 1990; Emmanuel and Day-

599   Stirrat 2012), the reduction of pores in sedimentary rocks during compaction is size-dependent - larger pores

600   deform much readily than smaller pores. According to their model, larger pores rapidly decrease in size during

601   compaction to reduce the overall porosity of the sample. However, microstructural analysis of Sumatra samples

602   suggests that porosity reduction is accomplished by compaction of all pore sizes. Moreover, the maximum size

603   of pores remains almost constant irrespective of increasing vertical effective stress/depth (Supplementary data-8)

604   with little difference observed for the maximum pore size in samples from 98.25 mbsf and 1299.31 mbsf. The

605   preservation of a constant ratio between MAD and BIB-SEM porosity measurements (Fig. 3b) suggests that

606   porosity loss is distributed across all pore sizes. We infer that all pore sizes are available for compaction for

607   every increment of applied stress but acknowledge that pore size reduction in different size classes may proceed

608   at different rates.

609   We propose a new model for the reduction in porosity in which all pores within the force chain of load take part

610   in the reduction of porosity during compaction irrespective of their size. At shallow depth up to 28mbsf, larger

611   clay-domain pores are the most susceptible to early response during an increase in compactional strain, because

612   of two reasons: 1) the 'domains' defined by the clay particles are weaker compared to the larger, rigid silt grains,

613   and 2) due to higher relative proportion of clay-rich regions within the mud, the force chain of load dominantly

614   passes through the clay domains. The dispersed nature of the silt-size particles and the high proportion of

615   phyllosilicates in the mud samples indicate that soft clay particles act as the principal load-bearing framework.

616   Hence, larger clay domain pores are more unstable compared to silt-adjacent pores in the mud microstructure.

617   Similarly, below 28mbsf depth, under an increase in vertical effective stress, both the larger silt-adjacent pores

618   and smaller pores in the clay matrix that come within the force chain of load collapse. Hence, the ratio between

619   BIB-SEM porosity vs MAD porosity remains almost constant irrespective of the depth. All larger silt-adjacent

620   pores do not come within the force chain of load at the same time. Hence, some of the larger silt-adjacent pores

621   remained undeformed to the maximum depth of 1500 mbsf depth. Therefore, the maximum size of the larger silt-

622   adjacent pores remains almost constant irrespective of the depth/vertical effective stress.

623   In this study, we investigated how systematically pore types evolve with increasing depth in naturally compacted

624   samples. However, tracking the pore evolution through additional size categories would elucidate the pore

625   evolution in more detail. Preliminary pore size distribution data (Fig.9) indicate that 4 size bins exist in these

626   samples. Developing this approach requires improved image analysis techniques to tie all the pore attributes

627   together on a pore-by-pore basis for a huge number of pores.

628   **5.4 Compaction strain accommodation and grain-scale deformation**

629   Deformation of clay-rich sedimentary rocks involves four possible mechanisms: 1) Particulate flow;

630   (Morgenstern and Tchalenko, 1967; Borradaile et al., 1981); 2) Cataclasis; (Ukar and Cloos, 2019) 3) Diffusive

631   mass transfer; (Blenkinsop, 2007; Fossen, 2016); 4) Intercrystalline plasticity (Blenkinsop, 2007; Fossen, 2016).

632   Intensity and occurrence of a particular deformation mechanism in a mudstone depend on several parameters,

633   such as effective stress, water content, cementation, temperature (Desbois et al., 2017; Den Hartog and Spiers,

634   2014).

635   All our samples show evidence of particulate flow controlled by friction between grains. At shallow depths,

636   illite platelets contacted at EE and EF junctions lose these weak bonds, and particles rotate into bedding-parallel

637   orientation. Once FF contacts dominate, large-scale rotations are reduced, and inter-particle slip becomes

638   important. This is best evidenced in collapse of large, silt-adjacent pores where bent clay particles overlay pores

639   (Fig.14a to f). In deforming granular foam material, bending was reported as the dominant deformation

640   mechanism for the reduction in porosity and developing preferred alignment of the long axis of pores

641   perpendicular to the applied stress (Elliott et al., 2002, Zhou et al., 2004; Samsudin et al., 2017; Zakaria et al.,

642   2018) (review of these earlier studies on the experimental deformation of granular foam is described in

643   document S2). Friction adheres clay particles to the edge of pores while the middle of particles drops into the

644   pore, resulting in bending by intra-particle slip. A cartoon (Fig.14g) illustrates the compaction mechanism

645   associated with the bending of clay particles. With increasing compaction strain, clay particles undergo bending,

646   and as a result, pore area reduces, and the orientation of the pores tends to align perpendicular to the applied

647   effective stress (Fig.14g). At shallow depths (Unit-I), particles get enough free space for rotation to align parallel

648   to the bedding plane because of higher porosity (Figure S12a and b). However, at greater depth where porosity

649   decreases, space problems limit particle deformation to bending and fracturing as increase in compactional strain

650   increases (Figure S12c and d).

651   5.5 Compaction of Sumatra input section: generalized implication for rock property evolution

652   The overall compaction curve obtained for Sumatra muds is comparable with the experimental study by Fawad

653   et al., 2010in the context of compactional range (Fig.8).The curve shows a mono-exponential decrease in

654   porosity with an increase in vertical effective stress, which is evidence of normal consolidation (Fawad et al.,

655   2010; Dutilleul et al., 2020).

656   The larger silt-adjacent pores seen in the deepest of these samples (1500 m burial) suggest these muds retain

657   considerable potential for additional mechanical compaction with deeper burial. As this marine sediment

658   progressively approaches greater burial closer to the accretionary prism, it will undergo further change in

659   physical and deformational properties (Bray and Karig, 1985). Despite the substantial compactional strain, the

660   relatively high porosity of the deepest sample and the survival of larger and mechanically unstable silt-margin

661   pores suggests that compactional stabilization has yet to be reached because such IGVs and pore types are not

662   generally observed in older and lithified mudrocks. Based on the current understanding of subduction zone

663   deformation behavior and mudrock properties, it seems likely that mechanical compaction will continue to

664   dominate the pore loss in deeper burial.

665   The general absence of early cementation and the corresponding dominance of mechanical compaction in the

666   total pore loss is consistent with observations of other siliciclastic-dominated muds (Milliken, 2014; 2019). The

667   trends for intergranular volume change observed from the seafloor and 1500 mbsf place useful constraints on the

maximum cement volumes that theoretically could be emplaced at this depth range in sediments containing a more reactive grain assemblage. At the depths of burial attained at the deformation front, any cementation of the Sumatra input sediments will be limited to <30% of the rock volume, or possibly much less, as mechanical compaction is expected to continue up to the burial temperatures that initiate grain reactions and associated cementation.

6. Conclusions

Pores are classified by size and microstructural position, resulting in a multi-modal contribution to the total porosity. Shallow samples (seafloor to 28 mbsf) display a sharp reduction in porosity from 80% to 52% as large clay domain/matrix pores collapse. Deeper samples (28 mbsf to 1500 mbsf) exhibit a smaller reduction in porosity from 50% to 32% due to the collapse of silt-adjacent pores by bending and subsequent fracturing/sliding of clay particles.

The class of large pores next to silt-sized grains (between 10^4 and 10^6 nm^2) remains common to >1 km burial, irrespective of the mineralogy of the silt-sized grains, but their size decreases with depth. Small, equant pores next to silt particles are abundant in the first 100 m of burial and remain common over the entire depth range.

Small pores in clay domains are almost all elongated, and abundant over all observed depths. Small, crescent-shaped elongate pores increase in abundance with depth as clay particles become folded by compactional processes.

The size-independence of pore loss arises because the force chain driving pore collapse is localized primarily within the volumetrically dominant and weaker clay-rich domains; larger pores around isolated silt particles enter into the force chain somewhat randomly and asynchronously and do not contribute preferentially to pore loss over the depth range studied.

An increase in effective stress up to 18MPa (~1500 mbsf) causes the development of weakly aligned phyllosilicate fabric (defined by mica and illite clay particles) in the microstructure.

Compaction processes in our samples are dominated by granular flow (rotation and frictional sliding of illite clay particles) at shallow depths. With increasing depth, compaction is additionally accommodated by bending of clay particles.

Data availability

High resolution SE2 and BSE images of all samples are available online at:

https://figshare.com/s/cbaada517b0b1409d575

Authors contributions

SL and KLM performed sample preparation and BIB-SEM microscopy. SL analysed the data. JLU and GD acquired funding. JLU managed the project. PV, KLM and JLU significantly contributed to interpret the data. SL

700 wrote the first draft of the manuscript. PV, KLM and JLU contributed for the correction and improvement of the
701 manuscript.

713 **References**

714 Adams, R. and Bischof, L.: Seeded region growing. IEEE Transactions on pattern analysis and machine
715 intelligence. IEEE: 16(6), 641-647. https//DOI. 10.1109/34.295913, 1994.

716 Ajdukiewicz, J. M. and Lander, R. H.: Sandstone reservoir quality prediction: state of the art, AAPG Bulletin,
717 94,: 1082-1091, https:// doi.org/10.1306/intro060110, 2010.

718 Ammon, C.J., Ji, C., Thio, H.K., Robinson, D., Ni, S., Hjorleifsdottir, V., Kanamori, H., Lay, T., Das, S.,
719 Helmberger, D. and Ichinose, G. Rupture process of the 2004 Sumatra-Andaman
720 earthquake, Science, 308(5725), 1133-1139,DOI: 10.1126/science.1112260, 2005.

721 Aplin, A.C. and Macquaker, J.H.: Mudstone diversity: Origin and implications for source, seal, and reservoir
722 properties in petroleum systems, AAPG bulletin, 95(12), 2031-2059, https://doi.org/10.1306/03281110162,
723 2011.

724 Aplin, A.C., Matenaar, I.F. and VvanDderPluijm, B.A.: Influence of mechanical compaction and chemical
725 diagenesis on the microfabric and fluid flow properties of Gulf of Mexico mudstones Journal of Geochemical
726 Exploration, 78, 449-451, https://doi.org/10.1016/S0375-6742(03)00035-9, 2003.

727 Aplin, A.C., Matenaar, I.F., McCarty, D.K. and Vvan Der Pluijm, B.A.: Influence of mechanical compaction and
728 clay mineral diagenesis on the microfabric and pore-scale properties of deep-water Gulf of Mexico mudstones,
729 Clays and Clay Minerals, 54(4), 500-514, https://doi.org/10.1346/CCMN.2006.0540411, 2006.

730 Backman, J., Chen, W., Kachovich, S., Mitchison, F. L.,Petronotis, K. E.,Yang, T. and Zhao, X.: Data report:
731 Revised age models for IODP Sites U1480 and U1481, Expedition 362, Proceedings of the International Ocean
732 Discovery Program, Expedition Reports 362, https://doi.org/10.14379/iodp.proc.362.202.2019, 2019.

733 Baruch, E.T., Kennedy, M.J., Löhr, S.C. and Dewhurst, D.N.: Feldspar dissolution-enhanced porosity in
734 Paleoproterozoic shale reservoir facies from the Barney Creek Formation (McArthur Basin, Australia). AAPG
735 Bulletin, 99(9), 1745-1770, https://doi.org/10.1306/04061514181, 2015.

736 Bennett, R.H., Bryant, W.R. and Keller, G.H.: Clay fabric of selected submarine sediments; fundamental
737 properties and models, Journal of Sedimentary Research, 51(1), 217-232, https://doi.org/10.1306/212F7C52-
738 2B24-11D7-8648000102C1865D, 1981.

739 Bennett, R.H., O'Brien, N.R. and Hulbert, M.H.: Determinants of clay and shale microfabric signatures:
740 processes and mechanisms. In Microstructure of Fine-Grained Sediments, 5-32, Springer, New York, NY.
741 https://DOI: 10.1007/978-1-4612-4428-8_2, 1991.

742 Blenkinsop, T.G.: Deformation microstructures and mechanisms in minerals and rocks, Springer Science &
743 Business Media, 2007.

744 Bowles, F.A., Bryant, W.R. and Wallin, C.: Microstructure of unconsolidated and consolidated marine
745 sediments, Journal of Sedimentary Research, 39(4), 1546-1551,https://doi.org/10.1306/74D71E7E-2B21-11D7-
746 8648000102C1865D, 1969.

747 Borradaile, G.J.: Particulate flow of rock and the formation of cleavage. Tectonophysics, 72(3-4), 305-321,
748 https://doi.org/10.1016/0040-1951(81)90243-2, 1981.

749 Bray, C.J. and Karig, D.E.: Porosity of sediments in accretionary prisms and some implications for dewatering
750 processes, Journal of Geophysical Research: Solid Earth, 90(B1), 768-778,
751 https://doi.org/10.1029/JB090iB01p00768, 1985.

752 Brown, K.M. and Ransom, B.: Porosity corrections for smectite-rich sediments: Impact on studies of
753 compaction, fluid generation, and tectonic history. Geology, 24(9), 843-846, https://doi.org/10.1130/0091-
754 7613(1996)024<0843:PCFSRS>2.3.CO;2, 1996.

755 Burland, J.B.: On the compressibility and shear strength of natural clays. Géotechnique, 40(3), 329-378,
756 doi.org/10.1680/geot.1990.40.3.329, 1990.

757 Chester, F.M., Rowe, C., Ujiie, K., Kirkpatrick, J., Regalla, C., Remitti, F., Moore, J.C., Toy, V., Wolfson-
758 Schwehr, M., Bose, S. and Kameda, J.:Structure and composition of the plate-boundary slip zone for the 2011
759 Tohoku-Oki earthquake. Science, 342(6163), 1208-1211, https://DOI: 10.1126/science.1243719, 2013.

760 Cetin, H.: Soil-particle and pore orientations during consolidation of cohesive soils. Engineering geology, 73(1-
761 2), 1-11, doi.org/10.1016/j.enggeo.2003.11.006, 2004.

Day-Stirrat, R.J., Aplin, A.C., Środoń, J. and Van der Pluijm, B.A.: Diagenetic reorientation of phyllosilicate minerals in Paleogene mudstones of the Podhale Basin, southern Poland, Clays and Clay Minerals, 56(1), 100-111, DOI: 10.1346/CCMN.2008.0560109, 2008.

Day-Stirrat, R.J., Flemings, P.B., You, Y., Aplin, A.C. and van der Pluijm, B.A.:The fabric of consolidation in Gulf of Mexico mudstones, Marine Geology, 295, 77-85, https://doi.org/10.1016/j.margeo.2011.12.003, 2012.

Day-Stirrat, R.J., Milliken, K.L., Dutton, S.P., Loucks, R.G., Hillier, S., Aplin, A.C. and Schleicher, A.M.: Open-system chemical behavior in deep Wilcox Group mudstones, Texas Gulf Coast, USA, Marine and Petroleum Geology, 27(9), 1804-1818, https://doi.org/10.1016/j.marpetgeo.2010.08.006, 2010.

Day-Stirrat, R.J., Schleicher, A.M., Schneider, J., Flemings, P.B., Germaine, J.T. and van der Pluijm, B.A.: Preferred orientation of phyllosilicates: Effects of composition and stress on resedimented mudstone microfabrics, Journal of Structural Geology, 33(9), 1347-1358, https://DOI:10.1016/j.jsg.2011.06.007, 2011.

Dean, S.M., McNeill, L.C., Henstock, T.J., Bull, J.M., Gulick, S.P., Austin, J.A., Bangs, N.L., Djajadihardja, Y.S. and Permana, H.: Contrasting décollement and prism properties over the Sumatra 2004–2005 earthquake rupture boundary, Science, 329(5988), 207-210, https://DOI: 10.1126/science.1189373, 2010.

Delage, P. and Lefebvre, G.: Study of the structure of a sensitive Champlain clay and of its evolution during consolidation. Canadian Geotechnical Journal, 21(1), 21-35, https://doi.org/10.1139/t84-003, 1984.

DellePiane, C., Almqvist, B.S., MacRae, C.M., Torpy, A., Mory, A.J. and Dewhurst, D.N.: Texture and diagenesis of Ordovician shale from the Canning Basin, Western Australia: Implications for elastic anisotropy and geomechanical properties. Marine and Petroleum Geology, 59, 56-71, doi.org/10.1016/j.marpetgeo.2014.07.017, 2015.

Den Hartog, S.A. and Spiers, C.J.: A microphysical model for fault gouge friction applied to subduction megathrusts, Journal of Geophysical Research: Solid Earth, 119(2), 1510-1529. https://doi.org/10.1002/2013JB010580, 2014.

Desbois, G., Urai, J.L. and Kukla, P.A.: Morphology of the pore space in claystones–evidence from BIB/FIB ion beam sectioning and cryo-SEM observations. eEarth Discussions, 4(1), 1-19, 2009.

Desbois, G., Urai, J.L., Hemes, S., Brassinnes, S., De Craen, M. and Sillen, X.: Nanometer-scale pore fluid distribution and drying damage in preserved clay cores from Belgian clay formations inferred by BIB-cryo-SEM. Engineering Geology, 179, 117-131, https://doi.org/10.1016/j.enggeo.2014.07.004, 2014.

Desbois, G., Höhne, N., Urai, J. L., Bésuelle, P., and Viggiani, G.: Deformation in cemented mudrock (Callovo–Oxfordian Clay) by microcracking, granular flow and phyllosilicate plasticity: insights from triaxial deformation, broad ion beam polishing and scanning electron microscopy, Solid Earth, 8, 291–305, https://doi.org/10.5194/se-8-291-2017, 2017.

794 Desbois, G., Urai, J. L., Kukla, P. A., Konstanty, J., &Baerle, C.: High-resolution 3D fabric and porosity model
795 in a tight gas sandstone reservoir: A new approach to investigate microstructures from mm-to nm-scale
796 combining argon beam cross-sectioning and SEM imaging. Journal of Petroleum Science and
797 Engineering, 78(2), 243-257, https://doi.org/10.1016/j.petrol.2011.06.004, 2011.

798 Djeran-Maigre, I., Tessier, D., Grunberger, D., Velde, B. and Vasseur, G.: Evolution of microstructures and of
799 macroscopic properties of some clays during experimental compaction. Marine and Petroleum Geology, 15(2),
800 109-128, doi.org/10.1016/S0264-8172(97)00062-7, 1998.

801 Dugan, B., McNeill, L. and Petronotis, K.: Expedition 362 preliminary report: Sumatra subduction zone,
802 International Ocean Discovery Program, 2017.

803 Dutilleul, J., Bourlange, S., Conin, M. and Géraud, Y.: Quantification of bound water content, interstitial
804 porosity and fracture porosity in the sediments entering the North Sumatra subduction zone from Cation
805 Exchange Capacity and IODP Expedition 362 resistivity data, Marine and Petroleum Geology, 111, 156-
806 165,.https://doi.org/10.1016/j.marpetgeo.2019.08.007, 2020.

807 Ehrenberg, S. N.: Assessing the relative importance of compaction processes and cementation to reduction of
808 porosity in sandstones: discussion. American Association of Petroleum Geologists Bulletin, 73, 1274-1276,
809 https://doi.org/10.1306/44B4AA1E-170A-11D7-8645000102C1865D, 1989.

810 Elliott, J.A., Windle, A.H., Hobdell, J.R., Eeckhaut, G., Oldman, R.J., Ludwig, W., Boller, E., Cloetens, P. and
811 Baruchel, J.: In-situ deformation of an open-cell flexible polyurethane foam characterised by 3D computed
812 microtomography, Journal of materials science, 37(8), 1547-1555, doi:10.1023/A:1014920902712,2002.

813 Emmanuel, S. and Day-Stirrat, R.J.:2012. A framework for quantifying size dependent deformation of nano-
814 scale pores in mudrocks Journal of applied geophysics, 86, 29-35, https://doi.org/10.1016/j.jappgeo.2012.07.011,
815 2012.

816 Fawad, M., Mondol, N.H., Jahren, J. and Bjørlykke, K.: Microfabric and rock properties of experimentally
817 compressed silt-clay mixtures, Marine and Petroleum Geology, 27(8), 1698-1712,
818 https://doi.org/10.1016/j.marpetgeo.2009.10.002, 2010.

819 Fossen, H.: Structural geology. Cambridge university press. 2016.

820 Ghosal, D., Singh, S.C. and Martin, J.:Shallow subsurface morphotectonics of the NW Sumatra subduction
821 system using an integrated seismic imaging technique, Geophysical Journal International, 198(3), 1818-1831,
822 https://doi.org/10.1093/gji/ggu182, 2014.

823 Griffiths, F.J. and Joshi, R.C.: Change in pore size distribution due to consolidation of
824 clays. Geotechnique, 39(1), 159-167, doi.org/10.1680/geot.1989.39.1.159, 1989.

825   Griffiths, F.J. and Joshi, R.C.: Clay fabric response to consolidation. Applied clay science, 5(1), 37-66,
826   doi.org/10.1016/0169-1317(90)90005-A, 1990.

827   Griffiths, F.J. and Joshi, R.C.: Change in pore size distribution owing to secondary consolidation of
828   clays. Canadian Geotechnical Journal, 28(1), 20-24, https://doi.org/10.1139/t91-003, 1991.

829   Hemes, S., Desbois, G., Klaver, J. and Urai, J.L.: Microstructural characterisation of the Ypresian clays (Kallo-
830   1) at nanometre resolution, using broad-ion beam milling and scanning electron microscopy. Netherlands Journal
831   of Geosciences, 95(3), 293-313, DOI: https://doi.org/10.1017/njg.2016.16, 2016.

832   Hemes, S., Desbois, G., Urai, J.L., De Craen, M. and Honty, M.: Variations in the morphology of porosity in the
833   Boom Clay Formation: insights from 2D high resolution BIB-SEM imaging and Mercury injection
834   Porosimetry. Netherlands Journal of geosciences, 92(4), 275-300, DOI: doi.org/10.1017/S0016774600000214,
835   2013.

836   Hemes, S., Desbois, G., Urai, J.L., Schröppel, B. and Schwarz, J.O.: Multi-scale characterization of porosity in
837   Boom Clay (HADES-level, Mol, Belgium) using a combination of X-ray μ-CT, 2D BIB-SEM and FIB-SEM
838   tomography. Microporous and mesoporous materials, 208, 1-20, https://
839   doi.org/10.1016/j.micromeso.2015.01.022, 2015.

840   Hesse, R.: Turbiditic and non-turbiditic mudstone of Cretaceous flysch sections of the East Alps and other
841   basins. Sedimentology, 22(3), 387-416, https://doi.org/10.1111/j.1365-3091.1975.tb01638.x, 1975.

842   Hippchen, S. and Hyndman, R.D.: Thermal and structural models of the Sumatra subduction zone: Implications
843   for the megathrust seismogenic zone. Journal of Geophysical Research: Solid Earth, 113(B12),
844   https://doi.org/10. https://doi.org/10.1002/2015TC003901,2008.

845   Ho, N.C., Peacor, D.R. and Van der Pluijm, B.A.: Preferred orientation of phyllosilicates in Gulf Coast
846   mudstones and relation to the smectite-illite transition. Clays and Clay Minerals, 47(4), 495-504,
847   DOI: 10.1346/CCMN. 1999.0470412, 1999.

848   Houben, M.E., Desbois, G. and Urai, J.L.: A comparative study of representative 2D microstructures in Shaly
849   and Sandy facies of Opalinus Clay (Mont Terri, Switzerland) inferred form BIB-SEM and MIP methods, Marine
850   and Petroleum Geology, 49, 143-161, https://doi.org/10.1016/j.marpetgeo.2013.10.009,. 2014.

851   Hüpers, A., Ikari, M.J., Dugan, B., Underwood, M.B. and Kopf, A.J.:Origin of a zone of anomalously high
852   porosity in the subduction inputs to Nankai Trough. Marine Geology, 361,147-162,
853   https://doi.org/10.1016/j.margeo.2015.01.004, 2015.

854   Hüpers, A., Torres, M.E., Owari, S., McNeill, L.C., Dugan, B., Henstock, T.J., Milliken, K.L., Petronotis, K.E.,
855   Backman, J., Bourlange, S. and Chemale, F.:Release of mineral-bound water prior to subduction tied to shallow
856   seismogenic slip off Sumatra. Science, 356(6340), 841-844. 2017.

857   Jiang, M., Klaver, J., Schmatz, J. and Urai, J.L.:Nanoscale porosity analysis in geological materials. Acta
858   Stereologica, 2015.

859   Kameda, A., Dvorkin, J., Keehm, Y., Nur, A. and Bosl, W.:Permeability-porosity transforms from small
860   sandstone fragments. Geophysics, 71(1), N11-N19, https://doi.org/10.1190/1.2159054, 2006.

861   Karaborni, S., Smit, B., Heidug, W., Urai, J. and Van Oort, E.: The swelling of clays: molecular simulations of
862   the hydration of montmorillonite. Science, 271(5252), 1102-1104, DOI: 10.1126/science.271.5252.1102, 1996.

863   Klaver, J., Desbois, G., Littke, R. and Urai, J.L.:BIB-SEM characterization of pore space morphology and
864   distribution in postmature to overmature samples from the Haynesville and Bossier Shales. Marine and
865   petroleum Geology, 59, 451-466, https://doi.org/10.1016/j.marpetgeo.2014.09.020, 2015.

866   Klaver, J., Desbois, G., Littke, R. and Urai, J.L.:BIB-SEM pore characterization of mature and post mature
867   Posidonia Shale samples from the Hils area, Germany. International Journal of Coal Geology, 158, 78-89,
868   https://doi.org/10.1016/j.coal.2016.03.003, 2016.

869   Klaver, J., Desbois, G., Urai, J.L. and Littke, R.:BIB-SEM study of the pore space morphology in early mature
870   Posidonia Shale from the Hils area, Germany. International Journal of Coal Geology, 103, 12-25.
871   https://doi.org/10.1016/j.coal.2012.06.012, 2012.

872   Kuila, U. and Prasad, M.:Specific surface area and pore-size distribution in clays and shales. Geophysical
873   Prospecting, 61(2-Rock Physics for Reservoir Exploration, Characterisation and Monitoring), pp.341-362,
874   https://doi.org/10.1111/1365-2478.12028,2013.

875   Lander, R. H. and Walderhaug, O. W.: Predicting porosity through simulating sandstone compaction and quartz
876   cementation.   American   Association   of   Petroleum   Geologists   Bulletin   83:   433-449,
877   https://doi.org/10.1306/00AA9BC4-1730-11D7-8645000102C1865D, 1999.

878   Lander, R. H., Larese, R. H. Larese and Bonnell, L. M.: Toward more accurate quartz cement models: The
879   importance of euhedral versus noneuhedral growth rates. American Association Petroleum Geologists Bulletin
880   92: 1537-1563. https://doi.org/10.1306/07160808037, 2008.

881   Laurich, B., Urai, J.L., Desbois, G., Vollmer, C. and Nussbaum, C.:Microstructural evolution of an incipient
882   fault zone in Opalinus Clay: Insights from an optical and electron microscopic study of ion-beam polished
883   samples from the Main Fault in the Mt-Terri Underground Research Laboratory. Journal of Structural
884   Geology, 67,107-128. https://doi.org/10.1016/j.jsg.2014.07.014, 2014.

885   Lay, T., Kanamori, H., Ammon, C. J., Nettles, M., Ward, S.N., Aster, R.C., Beck, S.L., Bilek, S.L., Brudzinski,
886   M.R., Butler, R. and DeShon, H.R.:The great Sumatra-Andaman earthquake of 26 Ddecember
887   2004. Sscience, 308(5725), pp.1127-1133, DOI: 10.1126/science.1112250, 2005.

888   Lazar, O.R., Bohacs, K.M., Macquaker, J.H., Schieber, J. and Demko, T.M.: Capturing key attributes of fine-

889   grained sedimentary rocks in outcrops, cores, and thin sections: nomenclature and description guidelines. Journal

890   of Sedimentary Research, 85(3), pp.230-246, https://doi.org/10.2110/jsr.2015.11, 2015.

891   Lundegard, P. D.: Sandstone porosity loss--a 'big picture' view of the importance of compaction. Journal of

892   Sedimentary Petrology 62: 250-260, https://doi.org/10.1306/D42678D4-2B26-11D7-8648000102C1865D, 1992.

893   March, A.: Mathematical theory of the Korngestah control for affine deformation. Journal of Crystallography-

894   Crystalline Materials , 81 (1-6), 285-297, doi.org/10.1524/zkri.1932.81.1.285, 1932.

895   McNeill, L.C., Dugan, B. and Petronotis, K.E., Backman, J., Bourlange, S., Chemale, F., Chen, W., Colson,

896   T.A., Frederik, M.C.G., Guèrin, G., Hamahashi, M., Henstock, T., House, B.M., Hüpers, A., Jeppson, T.N.,

897   Kachovich, S., Kenigsberg, A.R., Kuranaga, M., Kutterolf, S., Milliken, K.L., Mitchison, F.L., Mukoyoshi, H.,

898   Nair, N., Owari, S., Pickering, K.T., Pouderoux, H.F.A., Yehua, S., Song, I., Torres, M.E., Vannucchi, P.,

899   Vrolijk, P.J., Yang, T., and Zhao, X.: Sumatra Subduction Zone. Proceedings of the International Ocean

900   Discovery Program, 362, https://doi.org/10.14379/iodp.proc.362.102.2017, 2017a.

901   McNeill, L.C., Dugan, B. and Petronotis, K.E., Backman, J., Bourlange, S., Chemale, F., Chen, W., Colson,

902   T.A., Frederik, M.C.G., Guèrin, G., Hamahashi, M., Henstock, T., House, B.M., Hüpers, A., Jeppson, T.N.,

903   Kachovich, S., Kenigsberg, A.R., Kuranaga, M., Kutterolf, S., Milliken, K.L., Mitchison, F.L., Mukoyoshi, H.,

904   Nair, N., Owari, S., Pickering, K.T., Pouderoux, H.F.A., Yehua, S., Song, I., Torres, M.E., Vannucchi, P.,

905   Vrolijk, P.J., Yang, T., and Zhao, X.: Sumatra Subduction Zone. Proceedings of the International Ocean

906   Discovery Program, 362, (Supplementary material), https://doi.org/10.14379/iodp.proc.362supp.2017, 2017b.

907   Meade, R.H.: Removal of water and rearrangement of particles during the compaction of clayey sediments. US

908   Government Printing Office, 1964.

909   Mesri, G. and Olson, R.E.: Mechanisms controlling the permeability of clays. Clays and Clay minerals, 19(3),

910   151-158, 1971.

911   Milliken, K. L.: A compositional classification for grain assemblages in fine-grained sediments and sedimentary

912   rocks. Journal of Sedimentary Research 84: 1185-1199, https://doi.org/10.2110/jsr.2014.92, 2008.

913   Milliken, K. L.: A compositional classification for grain assemblages in fine-grained sediments and sedimentary

914   rocks. Journal of Sedimentary Research 84: 1185-1199, https://doi.org/10.2110/jsr.2014.92, 2014.

915   Milliken K. L.:Compactional and mass-balance constraints inferred from the volume of quartz cementation in

916   mudrocks. Mudstone Diagenesis: New Research Perspectives for Shale Hydrocarbon Reservoirs, Seals, and

917   Source Rocks. AAPG. 120: 33-48, DOI: 10.1306/13672209M121252, 2019.

918   Milliken, K. L. and Curtis, M. E.: Imaging pores in sedimentary rocks: Foundation of porosity prediction.

919   Marine and Petroleum Geology 73,: 590-608, https://doi.org/10.1016/j.marpetgeo.2016.03.020, 2016.

920   Milliken, K. L. and Day-Stirrat R. J.: Cementation in mudrocks: Brief review with examples from cratonic basin
921   mudrocks.   Memoir.   J.-Y.   Chatellier.   Tulsa,   Oklahoma,   USA,   AAPG,
922   https://doi.org/10.1306/13401729H55252,2013.

923   Milliken, K. L. and Olson, T.: Silica diagenesis, porosity evolution, and mechanical behavior in siliceous
924   mudstones, Mowry Shale Cretaceous, Rocky Mountains, U.S.A. Journal of Sedimentary Research 87: 366-387,
925   .https://doi.org/10.2110/jsr.2017.24, 2017.

926   Milliken, K. L., Rudnicki, M., Awwiller, D. N. and Zhang, T.: Organic matter-hosted pore system, Marcellus
927   Formation Devonian, Pennsylvania, USA. AAPG Bulletin 97: 177-200, https://doi.org/10.1306/07231212048,
928   2013.

929   Milliken, K.L. and Reed, R.M.: Multiple causes of diagenetic fabric anisotropy in weakly consolidated mud,
930   Nankai accretionary prism, IODP Expedition 316. Journal of Structural Geology, 32(12), 1887-1898,
931   doi.org/10.1016/j.jsg.2010.03.008, 2010.

932   Milliken, K. L., Esch, W. L., Reed, R. M. and Zhang. T.: Grain assemblages and strong diagenetic overprinting
933   in siliceous mudrocks, Barnett Shale Mississippian, Fort Worth Basin, Texas, U.S.A. AAPG Bulletin 96: 1553-
934   1578, https://doi.org/10.1306/12011111129, 2012.

935   Mitchell, J.K.:The fabric of natural clays and its relation to engineering properties. In Highway Research Board
936   Proceedings, 35, 1956.

937   Moeremans, R.E. and Singh, S.C.: Fore-arc basin deformation in the Andaman-Nicobar segment of the
938   Sumatra-Andaman subduction zone: Insight from high-resolution seismic reflection data, Tectonics, 34(8), 1736-
939   1750, doi.org/10.1002/2015TC003901, 2015.

940   Mondol, N.H., Bjørlykke, K., Jahren, J. and Høeg, K.: Experimental mechanical compaction of clay mineral
941   aggregates—Changes in physical properties of mudstones during burial. Marine and petroleum geology, 24(5),
942   289-311, https://doi.org/10.1016/j.marpetgeo.2007.03.006, 2007.

943   Morgenstern, N.R. and Tchalenko, J.S.: Microstructural observations on shear zones from slips in natural clays,
944   1967.

945   Nakano, R.: On weathering and change of properties of tertiary mudstone related to landslide. Soils and
946   Foundations, 7(1),1-14, https://doi.org/10.3208/sandf1960.7.1,1967.

947   Neagu, R.C., Cartwright, J. and Davies, R.:Measurement of diagenetic compaction strain from quantitative
948   analysis   of   fault   plane   dip. Journal   of   Structural   Geology, 32(5),   641-655,
949   https://doi.org/10.1016/j.jsg.2010.03.010, 2010.

950   Nole, M., Daigle, H., Milliken, K.L. and Prodanović, M.:A method for estimating microporosity of fine‑grained
951   sediments and sedimentary rocks via scanning electron microscope image analysis. Sedimentology, 63(6),1507-
952   1521, https://doi.org/10.1111/sed.12271, 2016.

953   Nollet, S., Hilgers, C. and Urai, J.: Sealing of fluid pathways in overpressure cells: a case study from the
954   Buntsandstein in the Lower Saxony Basin (NW Germany). International Journal of Earth Sciences, 94(5), 1039-
955   1055, https://doi.org/10.1007/s00531-005-0492-1, 2005.

956   Oelker, A.: Deformation properties of Boom Clay: Implementation of a multi-scale concept. Dissertation,
957   Rheinisch-WestfälischeTechnische Hochschule Aachen, DOI: 10.18154/RWTH-2019-09913, 2019.

958   Oertel, G. and Curtis, C.D.: Clay-ironstone concretion preserving fabrics due to progressive
959   compaction. Geological Society of America Bulletin, 83(9), 2597-2606, https://doi.org/10.1130/0016-
960   7606(1972)83[2597:CCPFDT]2.0.CO;2,1972.

961   Paxton, S. T., J. O. Szabo, J. M. Adjukiewicz and R. E. Klimentidis.: Construction of an intergranular volume
962   compaction curve for evaluating and predicting compaction and porosity loss in rigid-grain sandstone reservoirs.
963   American Association of Petroleum Geologists Bulletin 86: 2047-2067, https://doi.org/10.1306/61EEDDFA-
964   173E-11D7-8645000102C1865D, 2002.

965   Pickering, K.T., Carter, A., Andò, S., Garzanti, E., Limonta, M., Vezzoli, G. and Milliken, K.L.: 2020.
966   Deciphering relationships between the Nicobar and Bengal submarine fans, Indian Ocean. Earth and Planetary
967   Science Letters, 544, 116329, https://doi.org/10.1016/j.epsl.2020.116329, 2020.

968   Pommer, M. E. and Milliken, K. L.: Pore types and pore-size distributions across thermal maturity, Eagle Ford
969   Formation, South Texas. AAPG Bulletin 99: 1713-1744, https://doi.org/10.1306/03051514151, 2015.

970   Prawirodirdjo, L., Bocl, Y., McCaffrey, R., Genrich, J., Calais, E., Stevens, C., Puntodewo, S.S.O., Subarya, C.,
971   Rais, J., Zwick, P. and Fauzi, R.M.: Geodetic observations of interseismic strain segmentation at the Sumatra
972   subduction zone. Geophysical research letters, 24(21), 2601-2604, https://doi.org/10.1029/97GL52691, 1997.

973   Rieke, H.H. and Chilingarian, G.V.: Compaction of argillaceous sediments. Elsevier, 1974.

974   Rosenberger, K., Underwood, M.B., Vrolijk, P. and Haines, S.: Data report: clay mineral assemblages in
975   hemipelagic sediments entering the Sumatra subduction zone, IODP Sites U1480 and U1481, Expedition
976   362. Expedition, 362, 1. 2020.

977   Samsudin, M.S.F., Ariff, Z.M. and Ariffin, A.: Deformation behavior of open-cell dry natural rubber foam:
978   Effect of different concentration of blowing agent and compression strain rate. In AIP Conference Proceedings,
979   1835, No. 1, 020007, AIP Publishing LLC, 2017.

980 Schmatz, J., Klaver, J., Jiang, M. and Urai, J.L.: Nanoscale morphology of brine/oil/mineral contacts in
981 connected pores of carbonate reservoirs: Insights on wettability from Cryo-BIB-SEM. SPE Journal, 22(05),
982 1374-1384, https://doi.org/10.2118/180049-PA, 2017.

983 Schneider, J., Flemings, P.B., Day-Stirrat, R.J. and Germaine, J.T.:Insights into pore-scale controls on mudstone
984 permeability   through   resedimentation   experiments. Geology, 39(11),   1011-1014,
985 https://doi.org/10.1130/G32475.1 , 2011.

986 Sintubin, M.: Clay fabrics in relation to the burial history of shales. Sedimentology, 41(6), 1161-1169,
987 https://doi.org/10.1130/G32475.1, 1994.

988 Terzaghi, K. and Peck, R.B.: Soil Mechanics. Engineering Practice. John Wiley and Sons, Inc., New York, 1948.

989 Torres, M. E., Milliken, K. L., A. Hüpers, J.H. Kim, S.G. Lee: Authigenic clays versus carbonate formation as
990 products of marine silicate weathering in the input sequence to the Sumatra Subduction Zone, Gechemistry,
991 Geophysics Geosystems, 23 (4), https://doi.org/10.1029/2022GC010338, 2022.

992 Ukar, E. and Cloos, M.: Cataclastic deformation and metasomatism in the subduction zone of mafic blocks-in-
993 mélange, San Simeon, California, Lithos, 346, 105116, https://doi.org/10.1016/j.lithos.2019.06.018, 2019.

994 Underwood, M. B., N. Lawler, and K. McNamara.: Data report: standard mineral mixtures, normalization
995 factors, and determination of error for quantitative X-ray diffraction analyses of bulk powders and clay-sized
996 mineral   assemblages.   Proceedings   of   the   International   Ocean   Discovery   Program,   372,
997 doi.org/10.14379/iodp.proc.372B375.201.2020, 2020.

998 Vasseur, G., Djeran-Maigre, I., Grunberger, D., Rousset, G., Tessier, D. and Velde, B.: Evolution of structural
999 and physical parameters of clays during experimental compaction, Marine and petroleum geology, 12(8),
1000 pp.941-954, https://doi.org/10.1016/0264-8172(95)98857-2, 1995.

1001 Velde, B.: Compaction trends of clay-rich deep sea sediments, Marine Geology 133(3-4): 193-201,
1002 https://doi.org/10.1016/0025-3227(96)00020-5, 1996.

1003 Vrolijk, P.:On the mechanical role of smectite in subduction zones. Geology, 18(8), pp.703-707,
1004 https://doi.org/10.1130/0091-7613(1990)018<0703:OTMROS>2.3.CO;2, 1990.

1005 Wang, X., Jiang, Z., Jiang, S., Chang, J., Zhu, L., Li, X. and Li, J.: Full-scale pore structure and fractal
1006 dimension of the Longmaxi shale from the Southern Sichuan Basin: Investigations using FE-SEM, gas
1007 adsorption and mercury intrusion porosimetry. Minerals, 9(9), p.543, https://doi.org/10.3390/min9090543, 2019.

1008 Worden, R.H., Charpentier, D., Fisher, Q.J. and Aplin, A.C.: Fabric development and the smectite to illite
1009 transition in Upper Cretaceous mudstones from the North Sea: an image analysis approach. Geological Society,
1010 London, Special Publications, 249(1), 103-114, doi.org/10.1144/GSL.SP.2005.249.01.0, 2005.

1011 Yagiz, S.: Overview of classification and engineering properties of shales for design considerations.
1012 In Construction and Materials Issues 2001, 156-165, 2001.

1013 Zakaria, Z., Mohamad Ariff, Z. and Abu Bakar, A.: Monitoring deformation mechanism of foam cells in
1014 polyethylene foams via optical microscopy: Effect of density and microstructure. Journal of Cellular
1015 Plastics, 54(6), 957-976, https://doi.org/10.1177/0021955X18795035, 2018.

1016 Zhou, J., Shrotriya, P. and Soboyejo, W.O.: Mechanisms and mechanics of compressive deformation in open-
1017 cell Al foams. Mechanics of Materials, 36(8), 781-797, https://doi.org/10.1016/j.mechmat.2003.05.004,. 2004.
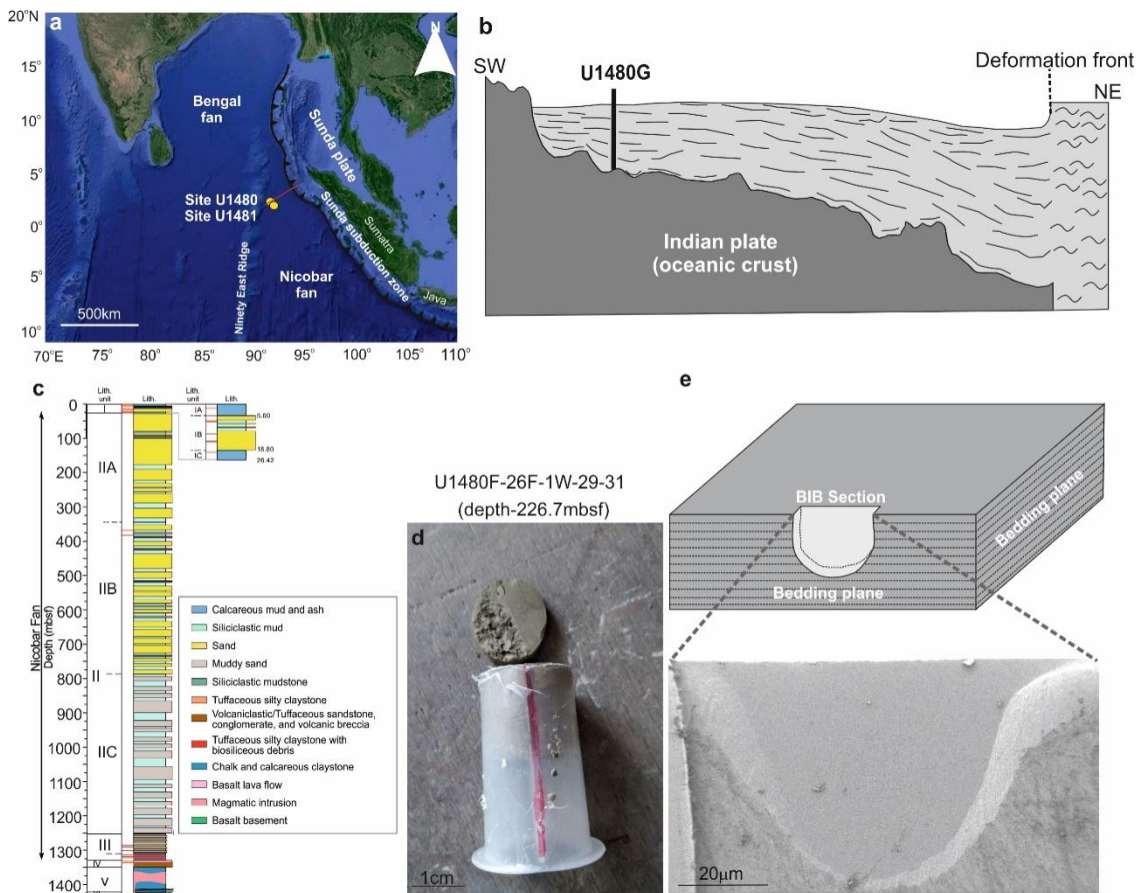
1018

1019

Fig.1: (a) Satellite image of Sumatra subduction zone and location of U1480 and U1481 drilling sites (created from © Google Maps). (b) Schematic diagram showing location of primary drilling site and deepest drill hole (Hole G) at site U1480 in sectional view (adapted from seismic profile from SW to NE after Hüpers et al., 2017). Location and extension of the seismic profile is represented by red line in (a). (c) Lithostratigraphic units encountered at Site U1480 (adapted after McNeill et al., 2017a). (d) Representative tube sample received from IODP repository, Japan. Red-colored line on tube surface represents notch used to denote orientation of samples collected from drill core. (e) Representative BIB cross-section polished perpendicular to bedding plane.
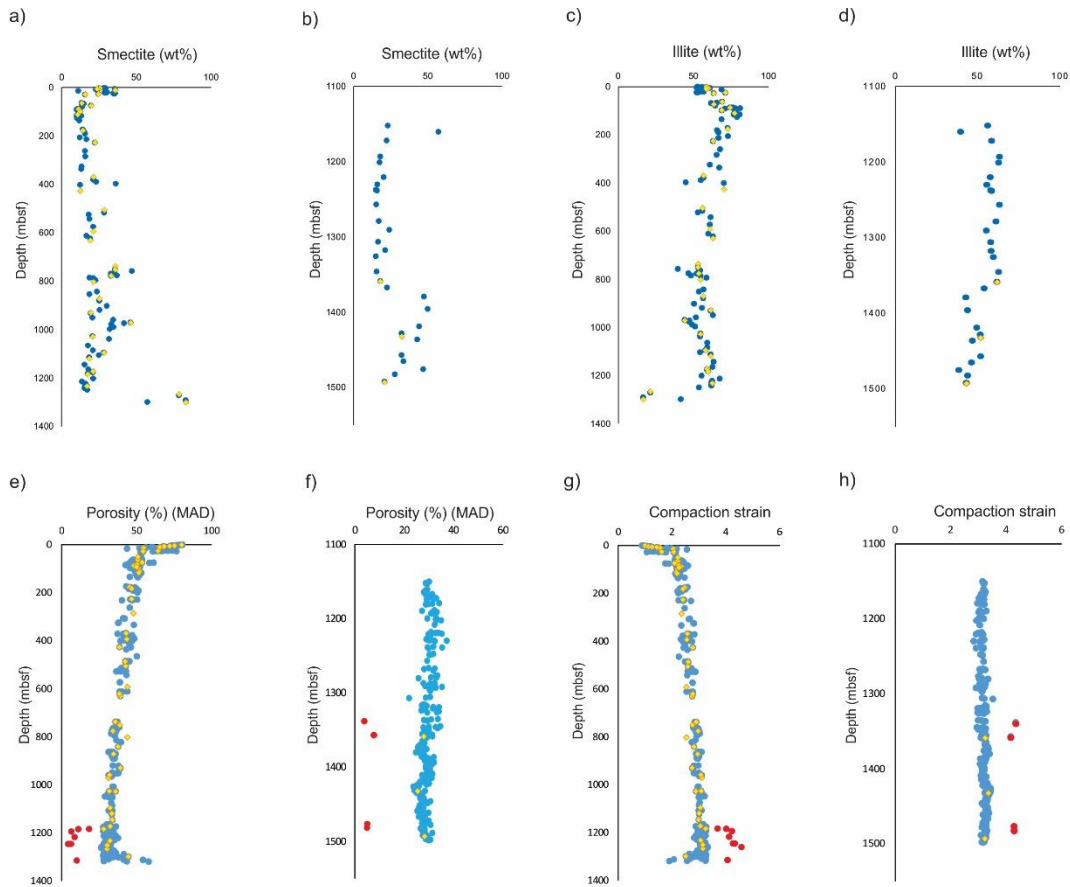
Fig.2: Depth profiles of smectite content (wt%; clay fraction) for Sites U1480 (a) and U1481 (b) (blue symbol). Depth profiles of illite content (wt%; clay fraction) for Sites U1480 (a) and U1481 (b) (blue symbol). Yellow symbols indicate samples analyzed by SEM imaging. (e) and (f) Shipboard MAD (Moisture and density) porosity profiles for mudstone samples recovered from Sites U1480 and U1481 (blue symbol). (g) and (h) Calculated compaction strain profiles for Sites U1480 and U1481 (blue symbols). Red-colored points are cemented (concretion) samples. Clay mineralogy data plotted from Rosenberger et al. (2020), and MAD data extracted from McNeill et al. (2017b).

1035

1036

1037

1038

1039

1040
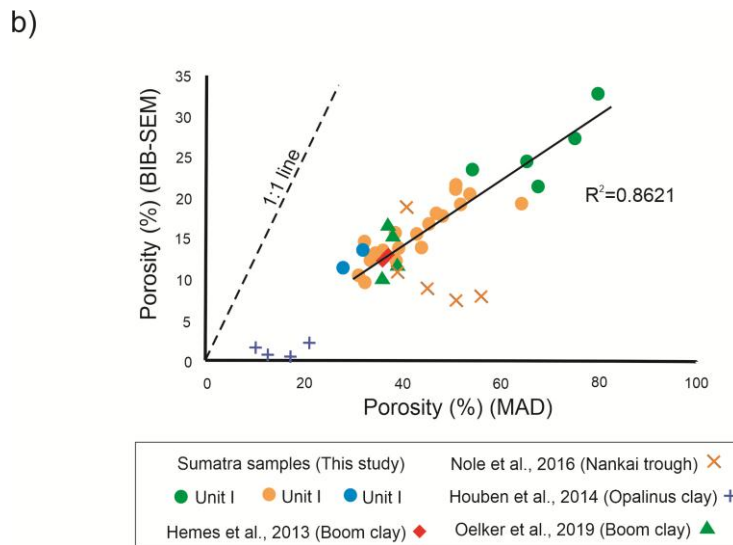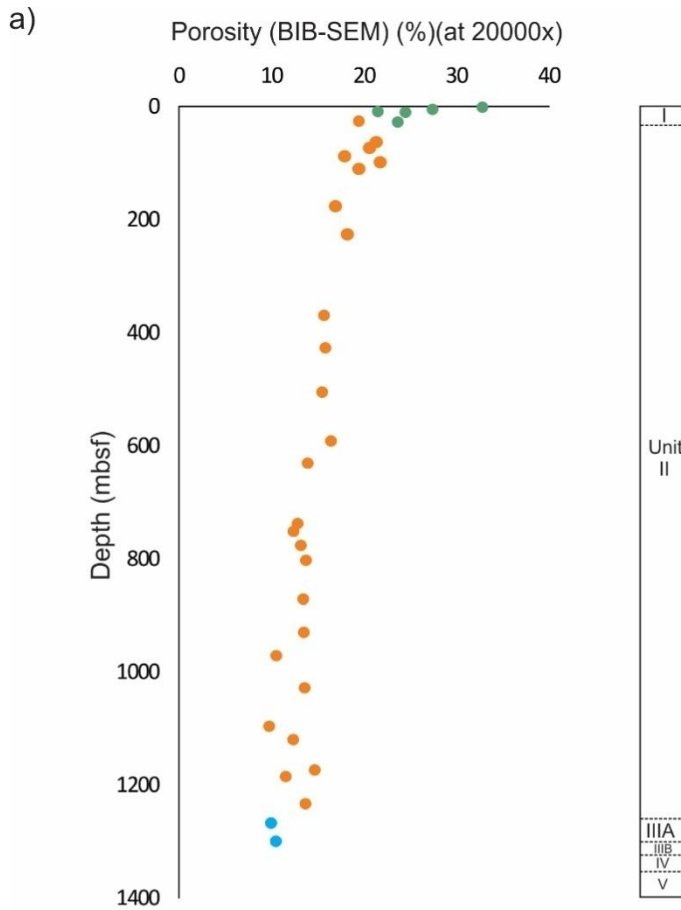
Fig.3: Porosity data for Units I (green dots), II (orange dots), and IIIA (blue dots). (a) BIB-SEM porosity - depth plot, (b) BIB-SEM porosity vs MAD porosity. Note: linear relationship that intersects origin. Data reported by Hemes et al. (2013); Houben et al. (2014); and Oelker et al. (2019) follow similar trend. However, data estimated from Nole et al. (2016) deviates from trend.
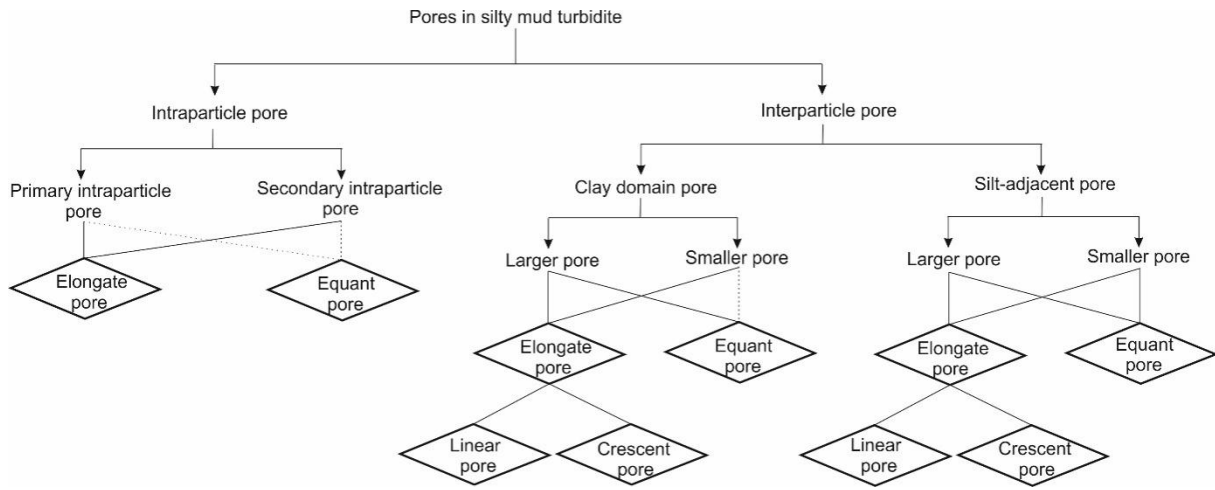
Fig.4: Classification scheme adopted to demonstrate pore reduction mechanics with increasing compactional strain. Dashed lines indicate rare pore types.

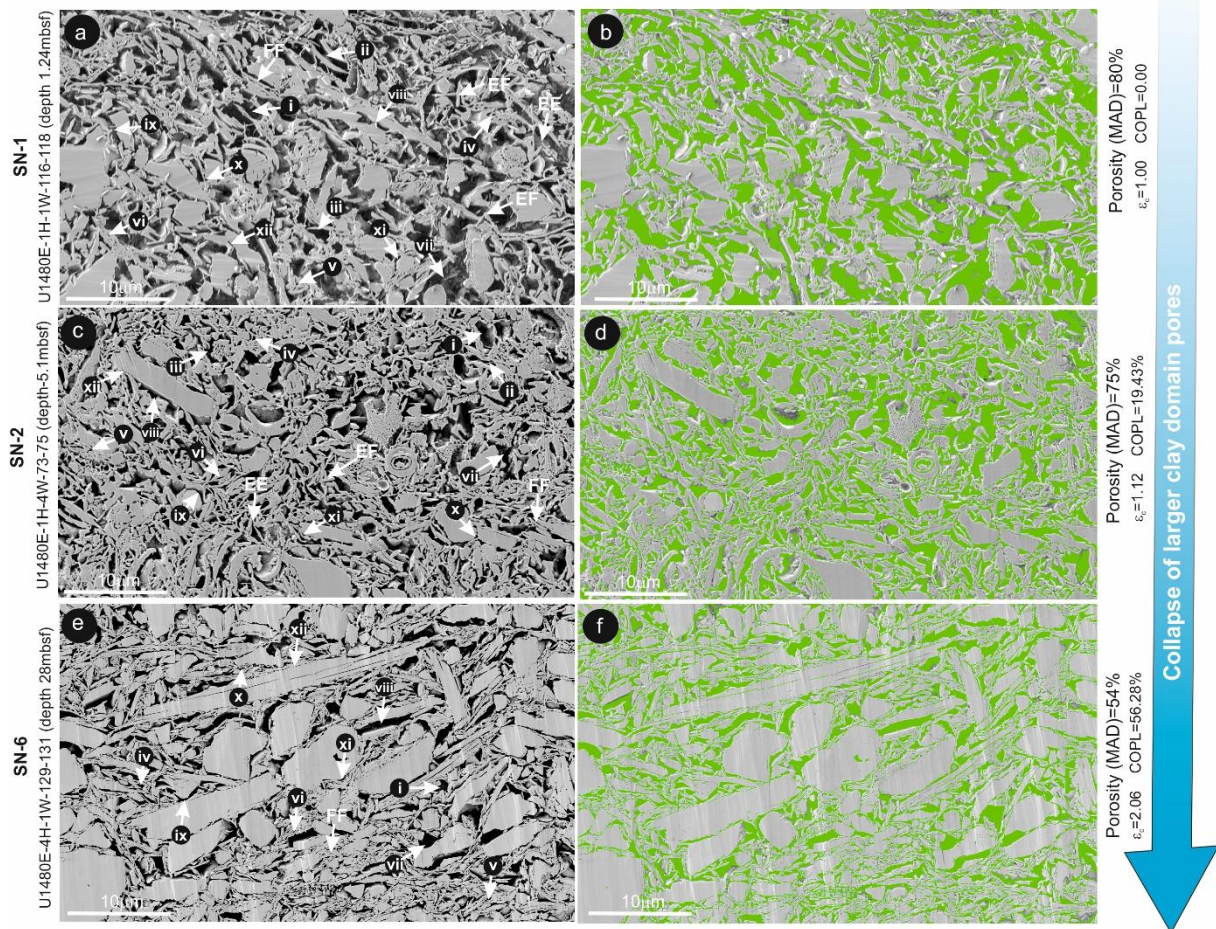**Fig.5:** Microstructural overview (BIB-SEM) of samples SN-1 (a and b), SN-2 (c and d), and SN-6 (e and f). Green color represents segmented pores of the corresponding microstructure of sample. i = Equant large clay domain pores, ii = elongated large clay domain pores, iii = Crescent-shaped large clay domain pores, iv = equant small clay domain pores, v = Crescent-shaped small clay domain pores, vi = elongated small clay domain pores, vii = Equant large silt-adjacent pores, viii = elongated large silt-adjacent pores, ix = Crescent-shaped large silt-adjacent pores, x =equant small silt-adjacent pores, xi = Crescent-shaped small silt-adjacent pores, xii = elongated small silt-adjacent pores. EE= Edge to edge contact, EF=Edge to face contact, and FF=Face to face contact.

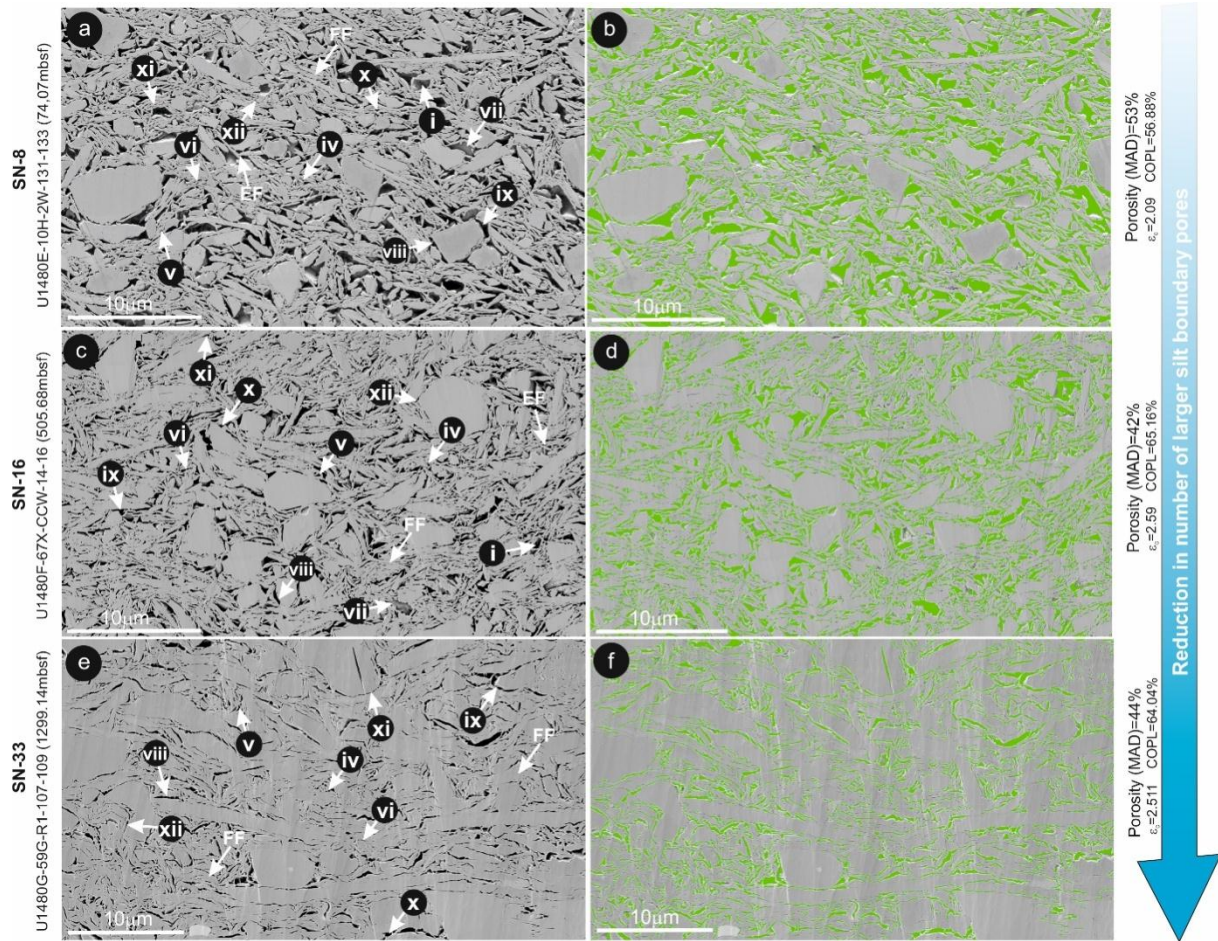**Fig.6:** Microstructural overview (BIB-SEM) of samples SN-8 (a and b), SN-16 (c and d), and SN-33 (e and f). Green color represents segmented pores of the corresponding microstructure of sample. i = Equant large clay domain pores, ii = elongated large clay domain pores, iii = Crescent-shaped large clay domain pores, iv = equant small clay domain pores, v = Crescent-shaped small clay domain pores, vi = elongated small clay domain pores, vii = Equant large silt-adjacent pores, viii = elongated large silt-adjacent pores, ix = Crescent-shaped large silt-adjacent pores, x =equant small silt-adjacent pores, xi = Crescent-shaped small silt-adjacent pores, xii = elongated small silt-adjacent pores. FF= Face to face contact, EF= Edge to face contact.

1092

1093

Fig.7: Microstructural overview (Field Emission SEM) of samples SN-34, SN-49, and SN-55. i = Equant large clay domain pores, ii =elongated large clay domain pores, iii = Crescent-shaped large clay domain pores, iv = equant small clay domain pores, v = Crescent-shaped small clay domain pores, vi = elongated small clay domain pores, vii = Equant large silt-adjacent pores, viii = elongated large silt-adjacent pores, ix = Crescent-shaped large silt-adjacent pores, x =equant small silt-adjacent pores, xi = Crescent-shaped small silt-adjacent pores, xii = elongated small silt-adjacent pores. FF= Face to face contact, EF= Edge to face contact.
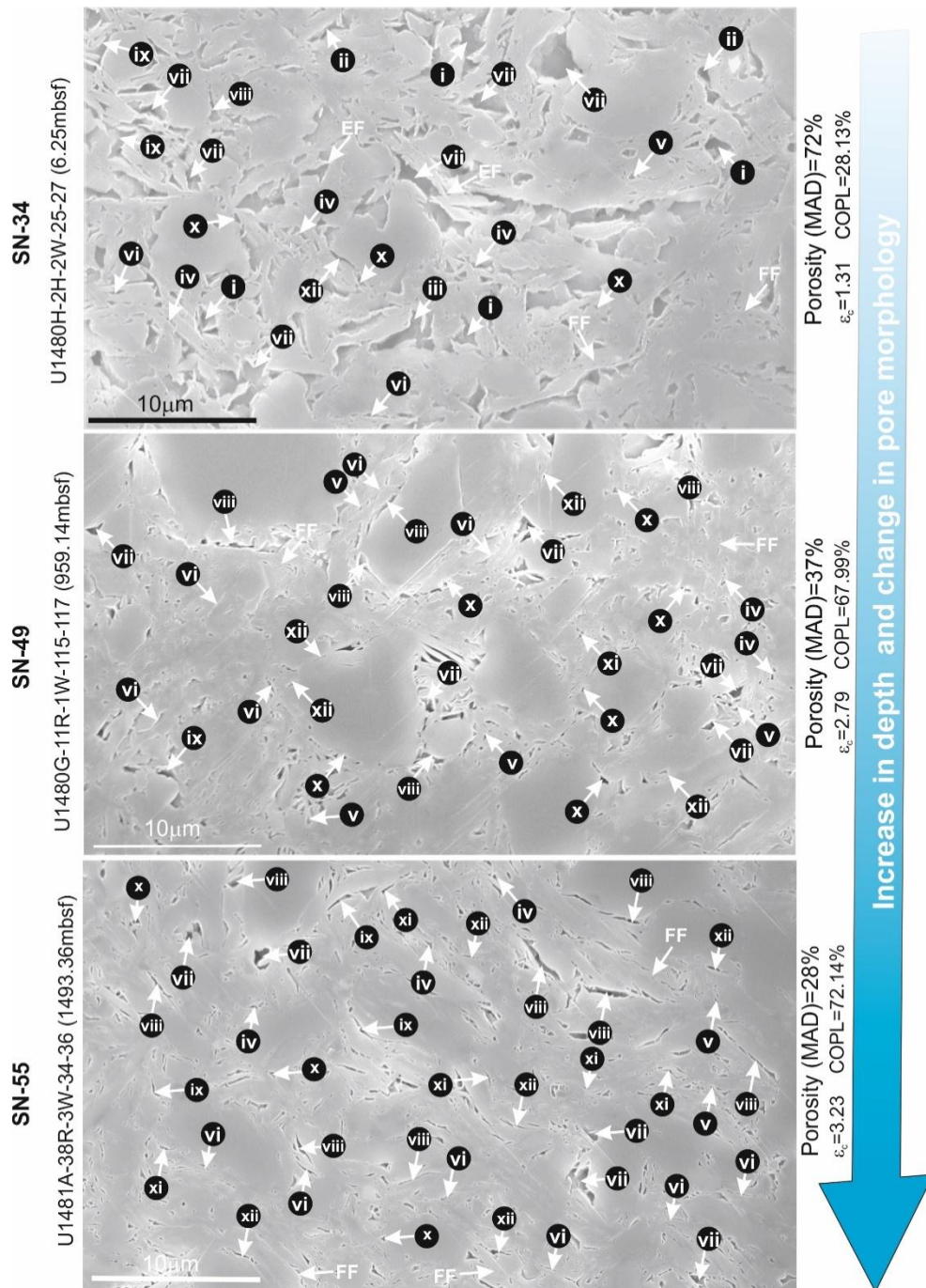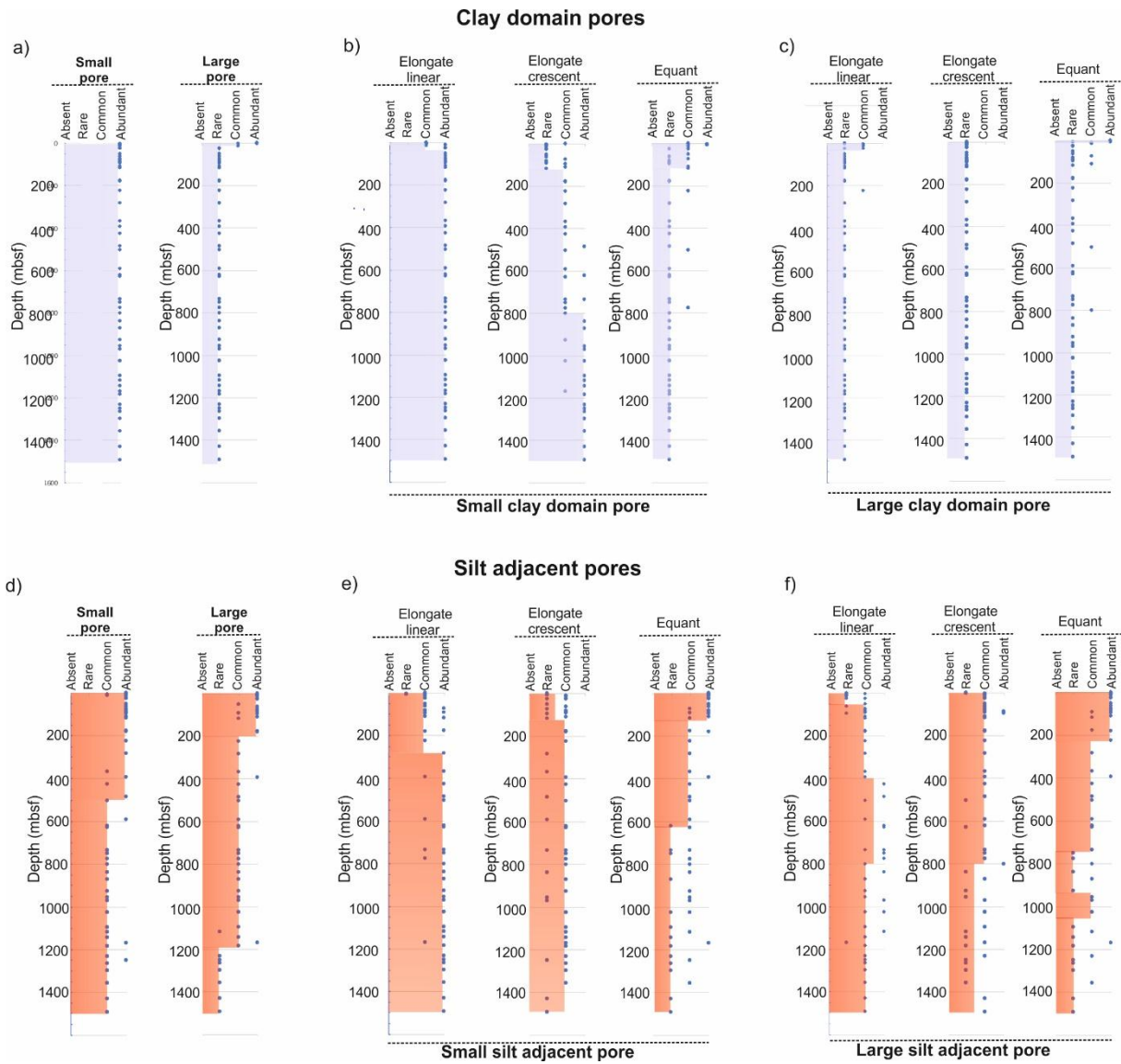
1100

1101

Fig.8: Pore type summary for clay domain (a-c) and silt-adjacent (d-f) pore types. (a) abundance of small and large clay domain pores; (b) and (c) depth progression of small and large clay domain pore morphologies; (d) abundance of small and large silt-adjacent pores; (e) and (f) depth progression of small and large clay domain pore morphologies. Abundant = >25% pores, common = 2%-25% pores, rare = 0-2% pores, absent = not observed.

1107

1108

1109

1110

1111

1112
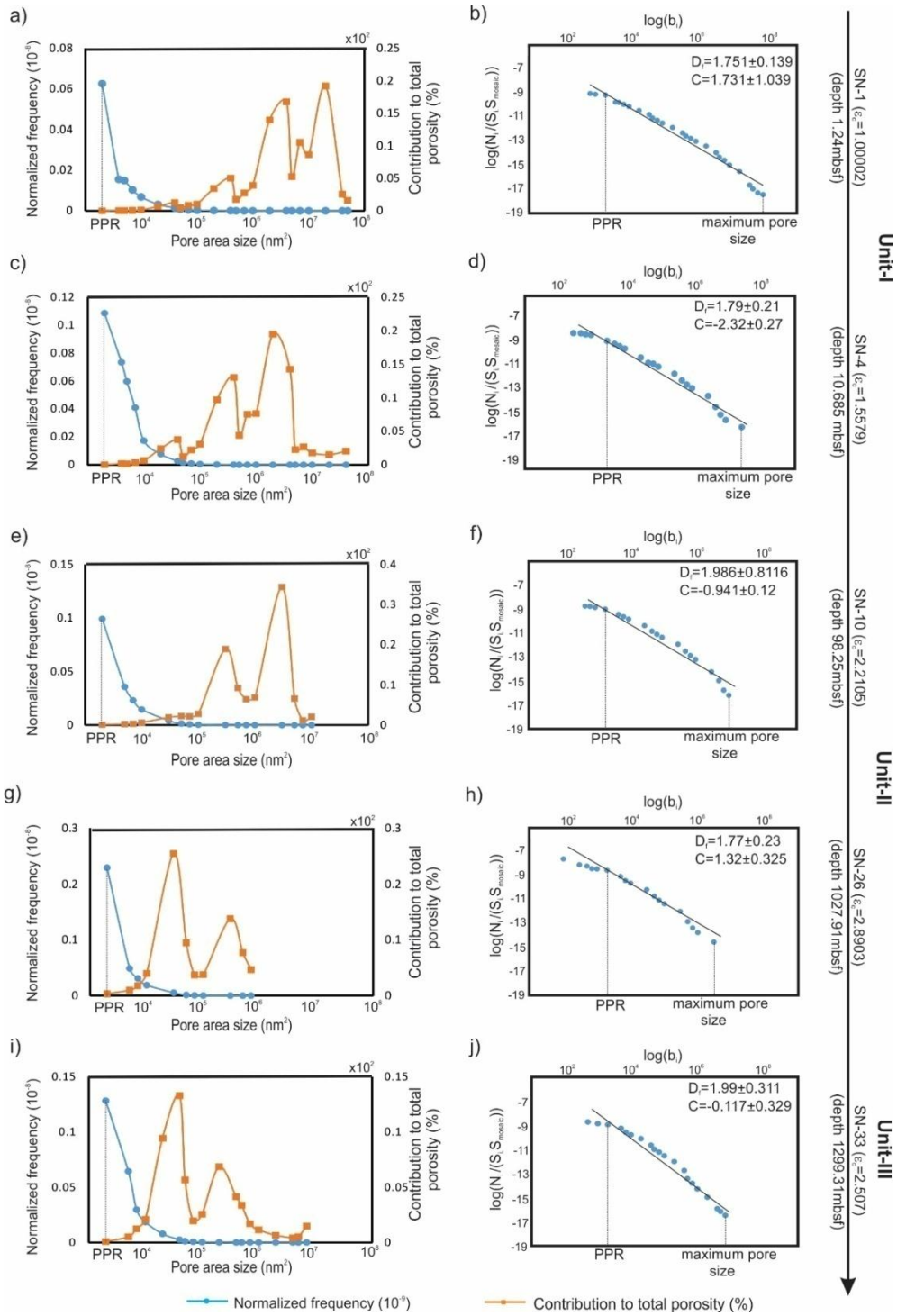
**Fig.9:** Pore size distribution defined by pore area. Left column: normalized frequency (blue) and contribution to total porosity (orange). Right column: pore size-frequency log-log distribution. Power-law between PPR and maximum pore size interpreted as black line with corresponding regression parameters. Sample number, depth, and compactional strain defined along right side of diagram

1117
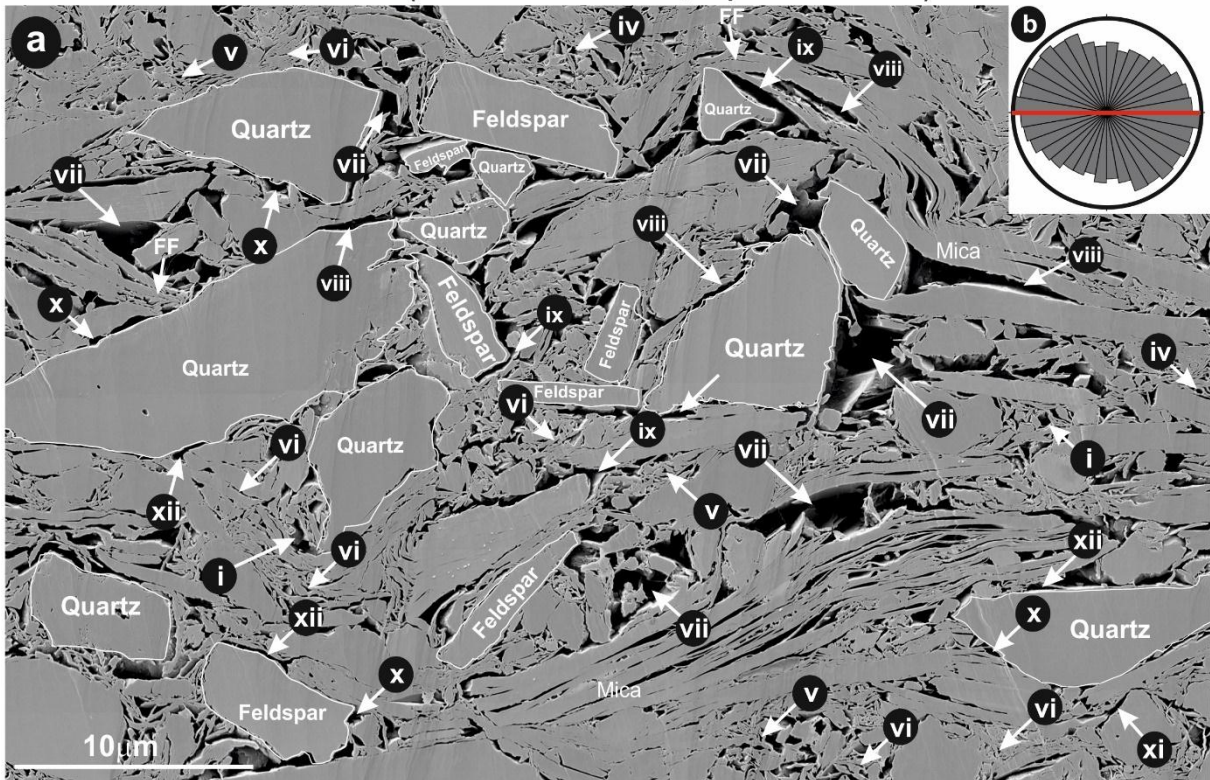
Fig.10: Silt-rich sample (SN-29; 1173 mbsf) (a) i = Equant large clay domain pores, ii =elongated large clay domain pores, iii = Crescent-shaped large clay domain pores, iv = equant small clay domain pores, v = Crescent-shaped small clay domain pores, vi = elongated small clay domain pores, vii = Equant large silt-adjacent pores, viii = elongated large silt-adjacent pores, ix = Crescent-shaped large silt-adjacent pores, x =equant small silt-adjacent pores, xi = Crescent-shaped small silt-adjacent pores, xii = elongated small silt-adjacent pores.(b) Rose diagram of long axes of pores (bedding = red line). FF= face to face contact of clay particles.

1126

1127

1128

1129
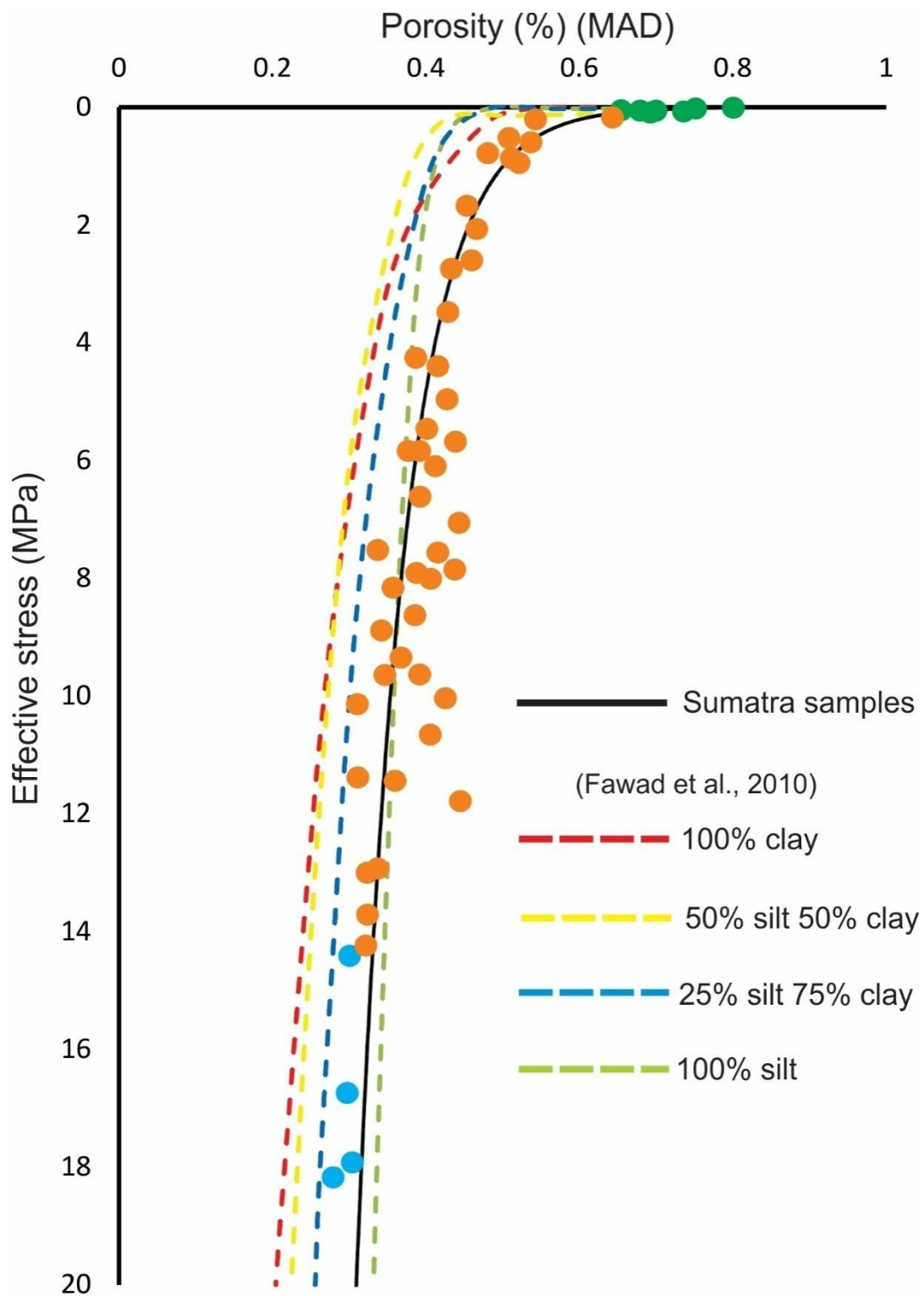
1130

Fig.11: Effective stress vs porosity (MAD) for experimental mixtures of clay and silt (dashed lines; Fawad et al., 2010) compared with Sumatra data (Unit 1 = green; Unit II = orange; Unit III = blue). Solid black solid line is a best-fit data regression for Sumatra samples.
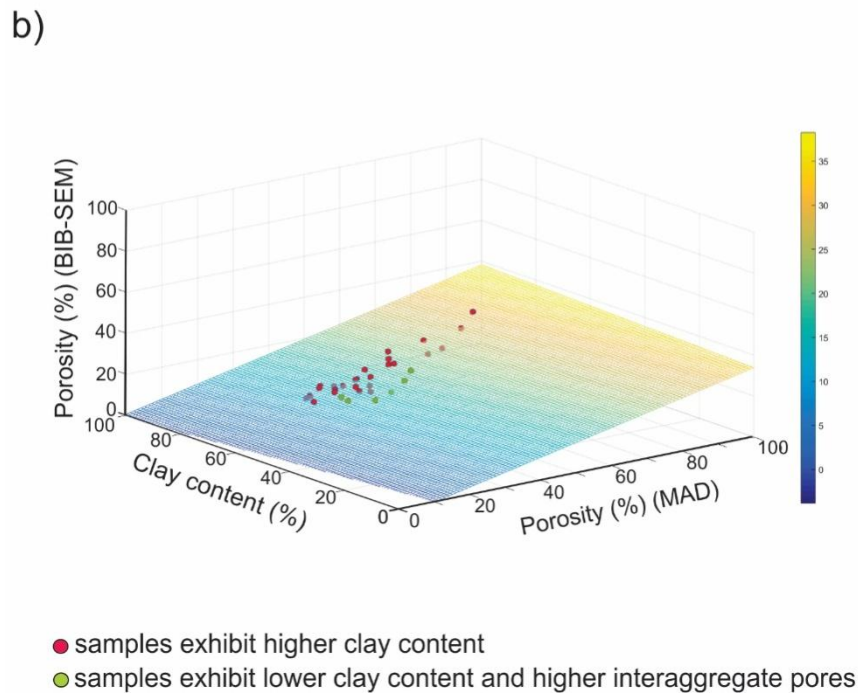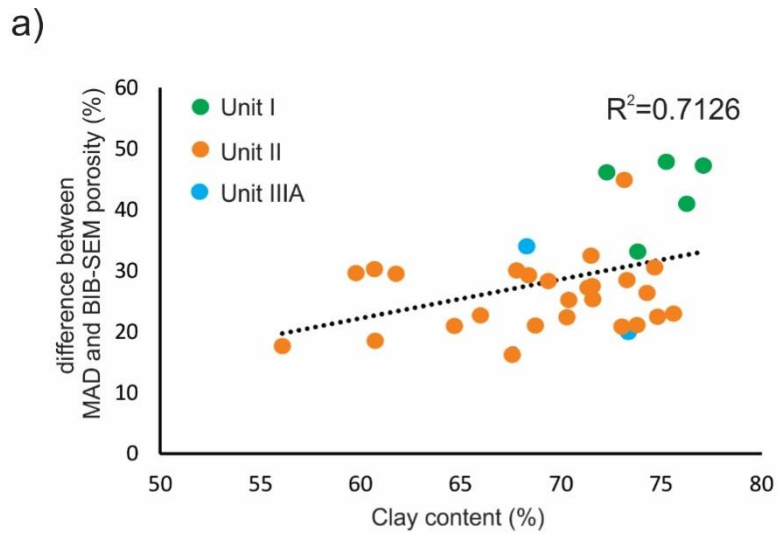
Fig.12: (a) Clay content vs difference between MAD and BIB-SEM porosity. Green, orange and blue colored symbols represent the samples from Unit-I, II and III respectively. (b) Multivariate regression analysis using three parameters: BIB-SEM porosity, clay content, and MAD porosity (33 samples).
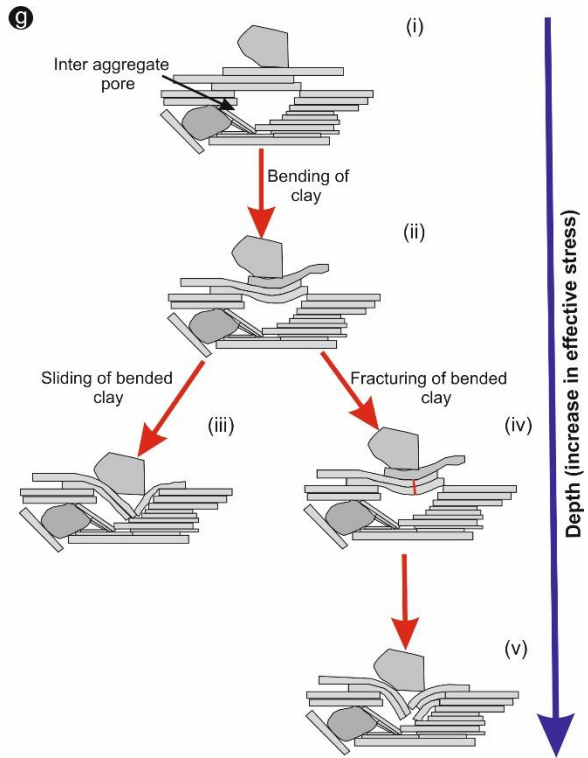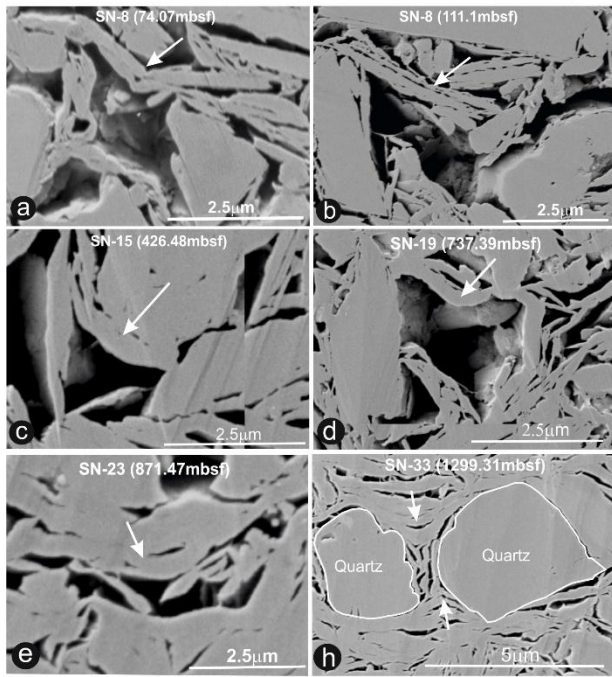
Fig.13: a-f: examples of bent clay particles on top of silt-adjacent larger pores; sample ID and depth labelled on photos. (g) Micromechanical model for collapse of large silt-adjacent pores.
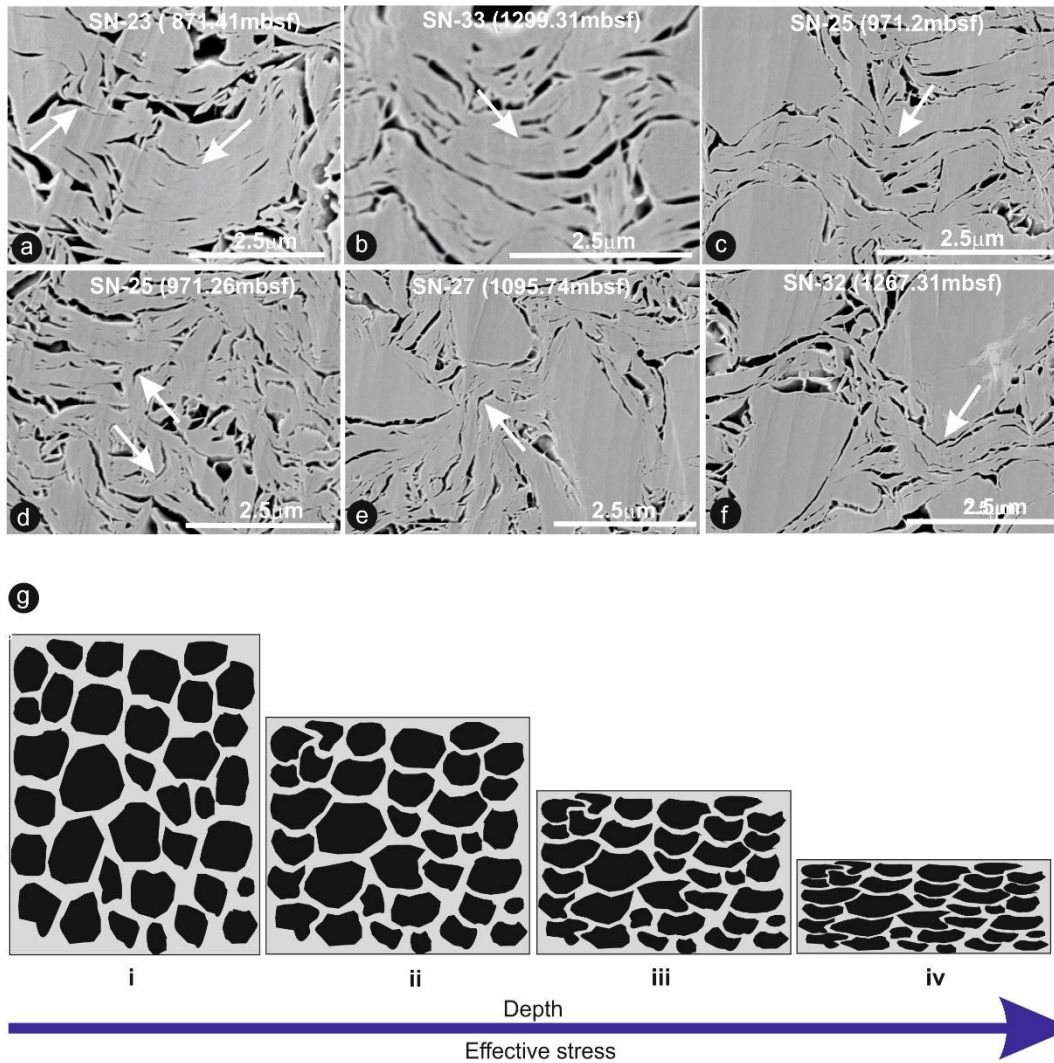
Fig.14: a-f: examples of clay aggregate bending (white arrows). (g) Conceptual diagram tracing porosity reduction and increase in preferred alignment of the long axes of pores by bending of clay perpendicular to applied vertical stress.

Table 1: Core description, bulk mineralogy (McNeill et al., 2017b) and clay composition (Rosenberger et al., 2020) of the analysed samples. Bulk measurements were done shipboard on Expedition 362 (McNeil et al., 2017a; Underwood, 2020). Additional clay mineralogical analysis was done on the <2μm particle fraction onshore using a different instrumentand methodology (Rosenberger et al., 2020). Here, Plag= Plagioclase feldspar, Smec= Smectite*, Chl= Chlorite, Kaol= kaolinite, Calc= Calcite.

|	Sample no	Site	Hole	Core	Type	Sec	Depth	Unit	Bulk mineralogical comp (XRD)				Clay mineralogical comp(XRD)			
									Total clay	Quartz	Plag.	Calc.	Smec*	Illite	Chl+Kaol	Quartz
First set of sample (Analysed at Aachen university)	SN-1	U1480	E	1	H	1	1.24	I	68	12	9	11	25	58	68	12
	SN-2	U1480	E	1	H	4	5.10	I	67	12	9	12	24	60	67	12
	SN-3	U1480	E	2	H	1	9.18	I	71	15	12	2	38	49	71	15
	SN-4	U1480	E	2	H	2	10.69	I	66	15	10	9	36	59	66	15
	SN-5	U1480	E	3	H	6	26.05	I	62	19	11	8	40	43	62	19
	SN-6	U1480	E	4	H	1	28.00	IIA	63	21	13	3	14	62	63	21
	SN-7	U1480	E	9	H	2	63.24	IIA	64	20	13	3	11	67	64	20
	SN-8	U1480	E	10	H	2	74.07	IIA	65	20	12	3	21	58	65	20
	SN-9	U1480	E	11	H	5	87.98	IIA	60	21	17	2	6	74	60	21
	SN-10	U1480	F	2	H	1	98.25	IIA	63	19	16	2	7	77	63	19
	SN-11	U1480	F	3	H	3	111.10	IIA	67	17	14	2	6	76	67	17
	SN-12	U1480	F	15	F	2	176.50	IIA	62	22	14	2	13	69	62	22
	SN-13	U1480	F	26	F	1	226.70	IIA	70	17	11	2	22	58	70	17
	SN-14	U1480	F	53	X	2	369.19	IIB	68	18	12	2	21	53	68	18
	SN-15	U1480	F	59	X	1	426.68	IIB	68	18	11	3	9	69	68	18
	SN-16	U1480	F	67	X	CC	505.32	IIB	70	17	11	1	30	49	70	17
	SN-17	U1480	F	76	X	1	592.42	IIB	61	24	12	3	22	56	61	24
	SN-18	U1480	F	80	X	CC	630.55	IIB	68	15	14	2	19	59	68	15
	SN-19	U1480	F	91	X	1	737.39	IIB	67	19	12	1	36	46	67	19
	SN-20	U1480	F	92	X	1	751.16	IIB	67	19	12	2	36	46	67	19
	SN-21	U1480	G	4	R	2	776.17	IIB	70	18	12	0	40	39	70	18
	SN-22	U1480	G	7	R	CC	802.55	IIC	62	23	14	2	23	54	62	23
	SN-23	U1480	G	14	R	2	871.87	IIC	66	21	12	2	28	50	66	21
	SN-24	U1480	G	20	R	1	929.81	IIC	67	19	11	3	21	57	67	19
	SN-25	U1480	G	24	R	3	971.26	IIC	66	19	13	1	41	40	66	19
	SN-26	U1480	G	30	R	2	1027.91	IIC	65	22	13	0	21	51	65	22
	SN-27	U1480	G	37	R	2	1095.74	IIC	68	19	12	1	30	51	68	19
	SN-28	U1480	G	41	R	1	1119.70	IIC	69	16	12	3	19	57	69	16
	SN-29	U1480	G	45	R	1	1172.88	IIC	63	21	11	5	22	54	63	21
	SN-30	U1480	G	46	R	3	1184.39	IIC	65	17	12	6	18	57	65	17
	SN-31	U1480	G	51	R	CC	1233.15	IIC	61	23	12	4	17	59	61	23
	SN-32	U1480	G	55	R	6	1267.14	IIIA	68	19	12	1	64	25	68	19
	SN-33	U1480	G	59	R	1	1299.31	IIIA	72	15	12	0	54	36	72	15
Second set of sample (Analysed at BEG)	SN-34	U1480	H	2	H	2	6.25	IB	71	18	11	0	25	54	19	2
	SN-35	U1480	E	1	H	6	7.21	IB	70	12	10	8	24	55	19	2
	SN-36	U1480	H	3	H	1	14.28	IB	62	21	14	3	5	70	9	15
	SN-37	U1480	E	4	H	1	28.12	IIA	63	21	13	2	14	62	11	14
	SN-38	U1480	E	7	H	1	50.82	IIA	61	22	14	3	11	67	15	7
	SN-39	U1480	H	10	H	2	83.02	IIA	59	21	15	4	6	74	10	10
	SN-40	U1480	H	16	H	1	117.13	IIA	62	20	16	2	12	73	11	5
	SN-41	U1480	E	12	H	2	92.82	IIA	59	23	16	2	6	72	9	13
	SN-42	U1480	F	16	F	3	182.62	IIA	64	21	13	2	14	63	16	7
	SN-43	U1480	F	37	X	2	285.51	IIA	66	20	12	2	15	62	19	4
	SN-44	U1480	F	55	X	5	394.01	IIB	58	28	13	0	40	38	13	9
	SN-45	U1480	F	65	X	CC	486.72	IIB	59	26	14	1	30	49	14	7
	SN-46	U1480	F	79	X	1	621.2	IIB	66	19	13	2	19	59	19	4
	SN-47	U1480	F	91	X	1	737.47	IIB	67	19	12	1	36	46	14	4
	SN-48	U1480	G	11	R	1	841.56	IIC	63	22	13	2	26	51	19	4
	SN-49	U1480	G	23	R	1	959.15	IIC	58	26	14	2	33	46	18	3
	SN-50	U1480	G	30	R	1	1026.34	IIC	68	18	12	2	21	51	24	3
	SN-51	U1480	G	42	R	3	1145.91	IIC	60	22	12	5	14	61	18	7
	SN-52	U1480	G	54	R	2	1251.5	IIIA	63	22	13	1	16	53	16	16
	SN-53	U1481	A	23	R	5	1358.9	IIC	68	17	11	3	18	58	20	4
	SN-54	U1481	A	32	R	1	1432.5	IIIA	65	23	11	1	32	46	17	5
	SN-55	U1481	A	38	R	3	1493.3	IIIA	60	26	13	1	20	42	14	24

*Smectite includes all mixed-layer I/S; expandability of mixed-layer I/S determined separately (Rosenberger et al., 2020).